PHYSICAL REVIEW B **93**, 165130 (2016)

Ohmic two-state system from the perspective of the interacting resonant level model: Thermodynamics and transient dynamics

H. T. M. Nghiem,[1] D. M. Kennes,[2] C. Klöckner,[2] V. Meden,[2,3] and T. A. Costi[1]

[1]*Peter Grünberg Institut and Institute for Advanced Simulation, Research Centre Jülich, D-52425 Jülich, Germany*

[2]*Institut für Theorie der Statistischen Physik, RWTH Aachen University and JARA–Fundamentals of Future Information Technology, 52056 Aachen, Germany*

[3]*Peter Grünberg Institut, Research Centre Jülich, D-52425 Jülich, Germany*

(Received 20 January 2016; revised manuscript received 6 April 2016; published 20 April 2016)

We investigate the thermodynamics and transient dynamics of the (unbiased) Ohmic two-state system by exploiting the equivalence of this model to the interacting resonant level model. For the thermodynamics, we show, by using the numerical renormalization group (NRG) method, how the universal specific heat and susceptibility curves evolve with increasing dissipation strength α from those of an isolated two-level system at vanishingly small dissipation strength, with the characteristic activatedlike behavior in this limit, to those of the isotropic Kondo model in the limit $\alpha \to 1^-$. At any finite $\alpha > 0$, and for sufficiently low temperature, the behavior of the thermodynamics is that of a gapless renormalized Fermi liquid. Our results compare well with available Bethe ansatz calculations at rational values of α, but go beyond these, since our NRG calculations, via the interacting resonant level model, can be carried out efficiently and accurately for *arbitrary* dissipation strengths $0 \leqslant \alpha < 1^-$. We verify the dramatic renormalization of the low-energy thermodynamic scale T_0 with increasing α, finding excellent agreement between NRG and density matrix renormalization group (DMRG) approaches. For the zero-temperature transient dynamics of the two-level system, $P(t) = \langle\sigma_z(t)\rangle$, with initial-state preparation $P(t \leqslant 0) = +1$, we apply the time-dependent extension of the NRG (TDNRG) to the interacting resonant level model, and compare the results obtained with those from the noninteracting-blip approximation (NIBA), the functional renormalization group (FRG), and the time-dependent density matrix renormalization group (TD-DMRG). We demonstrate excellent agreement on short to intermediate time scales between TDNRG and TD-DMRG for $0 \lesssim \alpha \lesssim 0.9$ for $P(t)$, and between TDNRG and FRG in the vicinity of $\alpha = \frac{1}{2}$. Furthermore, we quantify the error in the NIBA for a range of α, finding significant errors in the latter even for $0.1 \leqslant \alpha \leqslant 0.4$. We also briefly discuss why the long-time errors in the present formulation of the TDNRG prevent an investigation of the crossover between coherent and incoherent dynamics. Our results for $P(t)$ at short to intermediate times could act as useful benchmarks for the development of new techniques to simulate the transient dynamics of spin-boson problems.

DOI: 10.1103/PhysRevB.93.165130

I. INTRODUCTION

The Ohmic two-state model describes a quantum mechanical system tunneling between two states and subject to a coupling to environmental degrees of freedom [1,2]. It is a ubiquitous model in condensed matter physics, capable of describing, to varying degrees of approximation, the low-energy physics of a wide range of systems, including, for example, the tunneling of defects in solids [3,4], the diffusion of protons and muons in metals [5–7], or the quantum mechanical tunneling of fluxoid states in superconducting quantum interference devices [8]. Other possible realizations that have been proposed include two-level atoms in optical fibers [9] and, more recently, Cooper pair boxes, acting as two-level systems, and coupled to an electromagnetic environment consisting of an array of Josephson junctions [10–15]. Cooper pair boxes can host qubits with long coherence times $T_2 \sim 10{-}20\ \mu$s, and are currently being investigated [16] as one possible alternative to solid-state qubits [17] in the context of quantum information processing. The model also provides a microscopic starting point for describing electron transfer between donor and acceptor molecules in photosynthesis and other biological processes [18,19]. For an overview of the Ohmic two-state system, and quantum dissipative systems in general, see Ref. [20].

The Hamiltonian of the Ohmic two-state system, or the Ohmic spin-boson model (SBM), terms which we shall use interchangeably, is given by

$$H_{\rm SBM} = \underbrace{-\frac{1}{2}\Delta_0\sigma_x + \frac{1}{2}\epsilon\sigma_z}_{H_{\rm TLS}} + \underbrace{\frac{1}{2}\sigma_z\sum_i \lambda_i(a_i + a_i^\dagger)}_{H_{\rm int}} + \underbrace{\sum_i \omega_i(a_i^\dagger a_i + 1/2)}_{H_{\rm bath}}. \quad (1)$$

"Ohmic" refers to a particular choice of the couplings λ_i and oscillator frequencies ω_i, that we shall specify below. The first term $H_{\rm TLS}$ describes a two-level system with bias splitting ϵ and bare tunneling amplitude Δ_0, and $\sigma_{i=x,y,z}$ are Pauli spin matrices. The third term $H_{\rm bath}$ is the environment and consists of an infinite set of harmonic oscillators ($i = 1,2,\ldots,\infty$) with a_i ($a_i^\dagger$) the annihilation (creation) operators for a harmonic oscillator of frequency ω_i and $0 \leqslant \omega_i \leqslant \omega_c$, where ω_c is an upper cutoff frequency. The noninteracting density of states of the environment is denoted by $g(\omega) = \sum_i \delta(\omega - \omega_i)$ and is finite in the interval $[0,\omega_c]$ and zero otherwise. Finally, $H_{\rm int} = \frac{1}{2}\sigma_z\sum_i \lambda_i(a_i + a_i^\dagger)$ describes the

coupling of the two-state system coordinate σ_z to the oscillators, with λ_i denoting the coupling strength to oscillator i. The function $\Gamma(\omega+i\delta)=\sum_i \lambda_i^2/(\omega-\omega_i+i\delta)=\int d\omega'\lambda(\omega')^2\, g(\omega')/(\omega-\omega'+i\delta)$ characterizes the system-environment interaction. In particular, the spectral function $J(\omega)=-\frac{1}{\pi}\mathrm{Im}[\Gamma(\omega)]=\sum_i \lambda_i^2\delta(\omega-\omega_i)$ allows a classification of models into sub-Ohmic, Ohmic, and super-Ohmic depending on whether the low-frequency behavior of $J(\omega\to 0)\sim\omega^s$ is sublinear ($s<1$), linear ($s=1$), or superlinear ($s>1$).

In this paper, we shall be interested in the case of Ohmic dissipation ($s=1$), characterized by a spectral function $J(\omega)$ linear in frequency, $J(\omega)=2\pi\alpha\omega\theta(\omega_c-\omega)$, with α the dimensionless dissipation strength describing the strength of the coupling of the TLS to its environment. The Ohmic case is particularly interesting because, aside from its relevance to a large number of physical situations [20], it also allows for a mapping, in the scaling limit $\Delta_0/\omega_c\ll 1$, to a number of interesting fermionic models, including the anisotropic Kondo model (AKM), the spin-fermion model (SFM), and the interacting resonant level model (IRLM) [21–23]. Such equivalences prove to be very useful because powerful techniques developed for the fermionic models, such as the numerical renormalization group (NRG), can be used to investigate diverse properties of the Ohmic SBM, without restriction on temperature, coupling strength, or other system parameters.

More specifically, we shall use the equivalence of the Ohmic two-state system to the IRLM in order to (a) show explicitly that the IRLM can recover all the interesting regimes of the Ohmic two-state system, from zero ($\alpha=0$) to maximum dissipation strength ($\alpha\to 1^-$),[1] (b) shed further light on the thermodynamic properties of the former by application of the NRG to the latter, and (c) shed light on the accuracy of the recently developed time-dependent extension of the numerical renormalization group (TDNRG) for transient quantities [24–27] by comparison with complementary approaches, such as the TD-DMRG, the functional renormalization group (FRG), and the noninteracting-blip approximation (NIBA). For our purposes, a study of the unbiased Ohmic two-state system [i.e., $\epsilon=0$ in Eq. (1)] suffices. Apart from the NIBA, which yields unphysical results for transient dynamics at finite bias [20], the other methods can equally well be applied to finite bias also.

Historically, the main interest in the Ohmic two-state system has been to understand the crossover from coherent to incoherent dynamics of the two-level system as the coupling to the environment is increased [1,2,20,28]. Less attention has been given to thermodynamic properties (see Refs. [23,29–31]). While previous calculations for specific heats and dielectric susceptibilities of the Ohmic two-state system are available via the NRG and Bethe ansatz applied to the AKM [23,31], the results obtained using these methods remain incomplete: previous NRG calculations used a coarse temperature grid, such that the activated behavior of the specific heat for $\alpha\to 0$ was not well captured [31], while the Bethe ansatz results were readily available only at certain rational values of the dissipation strength $\alpha=1/\nu$ and $1-1/\nu$ for $\nu=2,3,4,\ldots$ due to the complexity of the thermodynamic Bethe ansatz equations for general α [23,32]. By implementing recent advances in the NRG [33,34], we are able to use a much finer temperature grid, thereby resolving all features in the specific heat with sufficient accuracy, even in the limit $\alpha\to 0$ (see Sec. IV A 1). More importantly, the equivalence of the IRLM to the Ohmic two-state system (1) allows calculations at *arbitrary* α to be carried out straightforwardly, in contrast to the limited values of α that are easily achievable within the Bethe ansatz. Thus, the IRLM results presented in this paper fill a gap in our quantitative understanding of the thermodynamics of the Ohmic two-state system. In addition, they demonstrate that the equivalence between the IRLM and the Ohmic two-state system is indeed valid for the whole range of dissipation strengths of interest. That such calculations are possible and yield meaningful results in the limit $\alpha\to 0$ is not immediately obvious since this limit corresponds to infinite Coulomb interaction in the IRLM (see Sec. II and Appendix A). Indeed, we shall show that the IRLM can describe the evolution of the thermodynamic properties of the Ohmic two-state system from the limit of an isolated two-level system at $\alpha=0$ to the limit of strong dissipation $\alpha\to 1^-$ where the universal scaling functions become those of the (isotropic) Kondo model. At the technical level, a further advantage in carrying out NRG calculations on the IRLM as opposed to the AKM (or the SFM) is that the former is spinless. This implies that a larger number of states can be retained within an NRG treatment of the IRLM than for the AKM (or the SFM), thereby allowing highly accurate results to be obtained for all dissipation strengths; the accuracy of these results will be demonstrated by comparison with limiting cases and Bethe ansatz calculations at representative values of α.

Beyond presenting results for thermodynamics at general values of α, and demonstrating that the IRLM can be applied to describe all regimes of interest of the Ohmic two-state system, the other main aim of this study is to shed light on the accuracy of the TDNRG for zero-temperature transient quantities at "short" to "intermediate times" (terms that we shall define precisely below). We do not address in any detail the $t\to 0^+$ limit of transient quantities, which is known to be exact in the TDNRG [26], nor the approach to the long-time limit $t\to\infty$ of transient quantities where finite errors appear (described in detail elsewhere [26,27]), but focus our attention on the accuracy of the TDNRG in the short to intermediate time range specified below. Such tests have so far been limited to cases with exact solutions [25–27]. It is therefore of some interest to assess the method for generic cases, such as for the Ohmic two-state system at arbitrary $\alpha>0$. For the latter, we shall focus attention on the quantity $P(t>0)=\langle\sigma_z(t)\rangle$, with initial-state preparation $\sigma_z(t\leqslant 0)=+1$, and assess the accuracy of the TDNRG results on short to intermediate time scales, i.e., on time scales $t\ll 1/\Delta_{\mathrm{eff}}(\alpha)$ and $t\sim 1/\Delta_{\mathrm{eff}}(\alpha)$, where $1/\Delta_{\mathrm{eff}}(\alpha)$ is a time scale that enters the transient dynamics within the NIBA [see Eq. (18) and Sec. IV B 1]. We distinguish here between intermediate times $t\sim 1/\Delta_{\mathrm{eff}}(\alpha)$ and long times $t\gg 1/\gamma_r(\alpha)$, where $\gamma_r(\alpha)$ sets

[1]We do not address the regime $\alpha>1$ since, in this regime, quantum mechanical tunneling is absent for most of the parameter space, a situation that can be addressed with perturbative methods.

the overall decay rate of $P(t)$. The decay rate $\gamma_r(\alpha)$ is of order $\alpha\Delta_{\rm eff}(\alpha)$ [20], implying that, for most α, except for $\alpha \ll 1$, the intermediate time scale $1/\Delta_{\rm eff}(\alpha)$ is also the relevant time scale for the approach to the long-time limit. For $\alpha \ll 1$, however, times t such that $1/\Delta_{\rm eff}(\alpha) \ll t < 1/\gamma_r(\alpha)$, should be regarded as intermediate times.[2] We shall directly compare TDNRG results with corresponding results from other approaches, such as with the NIBA, which is expected to be accurate at $\alpha \ll 1$ (on the time scales given above), with the functional renormalization group (FRG) (which is a controlled around $\alpha = \frac{1}{2}$), and with the time-dependent density matrix renormalization group (TD-DMRG) (valid for general α). Beyond demonstrating convincingly that the TDNRG is quantitatively accurate in the above time range and for the whole range of dissipation strengths $0 \lesssim \alpha \lesssim 0.9$, the comparisons will also allow us to quantify the errors in the NIBA in the regime where it is traditionally expected to be a reasonable approximation, i.e., for $0 \lesssim \alpha \lesssim \frac{1}{2}$ and $\epsilon = 0$. While many techniques have been developed to simulate the time-dependent dynamics of the spin-boson model [25,35–41], a quantitative test of the accuracy of the NIBA at zero temperature and in the above regime and time range has so far been lacking. We provide such a test by demonstrating quantitative differences between the TDNRG and the NIBA in the range $0.1 \lesssim \alpha \lesssim 0.4$ for times comparable to $1/\Delta_{\rm eff}(\alpha)$, where very much smaller differences are found between TDNRG and TD-DMRG. We shall also briefly discuss why the errors in the long-time limit $t \gg 1/\gamma_r(\alpha)$ of the TDNRG prevent an investigation of the recently revealed novel scenario for the crossover between coherent and incoherent dynamics upon increasing α [28,42,43].

We note that although the NRG has been developed [44,45] to deal directly also with models such as (1), where an impurity couples to a continuous bath of bosons (and possibly also to a fermionic bath), and applied to a number of such models [19,25,45–49], this "bosonic NRG" is not expected, in general, to be as accurate as the NRG applied to equivalent fermionic models. The reason for this is that each bosonic orbital in Eq. (1) can accommodate an infinite number of bosons, whereas fermionic orbitals accommodate only a single fermion (of given spin). Consequently, the truncation of the Hilbert space, which is inherent in the NRG procedure, is a more severe approximation for bosonic systems than for the equivalent fermionic ones. Indeed, we shall see in Sec. IV A that available bosonic NRG results for the specific heat of the Ohmic SBM, while qualitatively correct, are in quantitative disagreement with those obtained from both the IRLM and the Bethe ansatz. Therefore, our highly accurate results for thermodynamic properties of the Ohmic two-state system via the IRLM could act as motivation for future improvements of the bosonic NRG.

Finally, aside from the interest in the IRLM for applications to the Ohmic two-state system [50], the model is of interest in its own right [22,51–53]. The two-lead IRLM is of interest in understanding the role of interactions in the linear and nonlinear transport through correlated quantum dots [54–65], while the IRLM with multiple channels has recently been proposed as a starting point to explain the peculiar heavy-fermion state of some Sm skutterudite compounds [66].

The outline of the paper is as follows. In Sec. II, we describe the IRLM and its equivalence to the Ohmic two-state system and discuss some limiting cases. Details of the equivalence of the Ohmic two-state system to a number of fermionic models, including the IRLM, via bosonization may be found in Appendix A. Methods are briefly described in Sec. III. In Sec. IV A, we present NRG results for thermodynamic properties (specific heats, susceptibilities, and Wilson ratios), while in Sec. IV B, we present our TDNRG results for the time-dependent quantity $P(t)$, comparing them with the NIBA (in Sec. IV B 1), the TD-DMRG (in Sec. IV B 2) and the FRG (in Sec. IV B 3), with additional supportive results in Appendix B. We summarize with an outlook for future work in Sec. V.

II. INTERACTING RESONANT LEVEL MODEL AND CONNECTION TO THE OHMIC TWO-STATE SYSTEM

The interacting resonant level model (IRLM) is given by the following Hamiltonian:

$$H_{\rm IRLM} = \underbrace{\varepsilon_d n_d + V(f_0^\dagger d + d^\dagger f_0)}_{H_{\rm imp}} + \underbrace{U(n_d - 1/2)(n_0 - 1/2)}_{H_{\rm int}} + \underbrace{\sum_k \epsilon_k c_k^\dagger c_k}_{H_{\rm bath}} . \quad (2)$$

It describes a spinless resonant level with energy ε_d hybridizing with a spinless bath of conduction electrons (where we wrote $f_0 = \sum_k c_k$ and $n_0 = f_0^\dagger f_0$) and interacting with the latter via a Coulomb interaction U. The correspondence of the Ohmic SBM to this model is given by $\Delta_0 = 2V$, $\epsilon = \varepsilon_d$, and $\alpha = (1 + 2\delta/\pi)^2/2$ where $\delta = \arctan(-\pi\rho U/2)$ and $\rho = 1/2D$ is the density of states of the spinless conduction electrons with half-bandwidth D and the high-energy cutoffs of the two models are related by $\omega_c = 2D$. In the scaling limit $V/D = \Delta_0/\omega_c \ll 1$, the equivalence between the models can be shown via bosonization [21], and is valid for $-\infty \leqslant U \leqslant +\infty$ (describing the sector $2 \geqslant \alpha \geqslant 0$) (see Appendix A for a detailed derivation of this and related equivalences). In order to set some notation, we consider the limit of an isolated two-level system. First, note that the two states in the IRLM which comprise the two-level system in the SBM are the states $|\uparrow\rangle = |1\rangle_d|0\rangle_0$ and $|\downarrow\rangle = |0\rangle_d|1\rangle_0$, split by $\epsilon = \varepsilon_d$, and connected by the hybridization V which acts as the tunneling term in the SBM with $V = \Delta_0/2$. States $|0\rangle_d|0\rangle_0$ and $|1\rangle_d|1\rangle_0$ lie $U/2$ higher in energy and become decoupled, together with the band (except for the Wannier orbital f_0), in the limit $U \to \infty$. Hence, the isolated two-level system ($\alpha = 0$) corresponds to $U = +\infty$ in the IRLM and the eigenvalues are given by $E_\pm = \pm\frac{1}{2}\sqrt{\epsilon^2 + \Delta_0^2}$. The corresponding eigenstates, for $\epsilon = 0$, are given by $\Psi_\pm = \frac{1}{\sqrt{2}}(|\uparrow\rangle \pm |\downarrow\rangle)$. From the partition function $Z = 2\cosh(\frac{\beta}{2}\sqrt{\epsilon^2 + \Delta_0^2})$ and free energy $F = -k_{\rm B}T \ln Z$,

[2] In general, by $\Delta_{\rm eff}(\alpha)$ or $\gamma_r(\alpha)$ we mean the NIBA expressions for these quantities. However, in cases where the NIBA expressions become quantitatively inaccurate, such as at strong dissipation $\alpha > \frac{1}{2}$, we shall point this out.

we have the dielectric (or charge) susceptibility $\chi(T,\epsilon=0)$ and specific heat $C(T,\epsilon=0)$ of the symmetric two-level system,

$$\chi(T) = \frac{1}{2\Delta_0}\tanh(\beta\Delta_0/2), \tag{3}$$

$$C(T) = \left(\frac{\beta\Delta_0}{2}\right)^2 \mathrm{sech}^2(\beta\Delta_0/2), \tag{4}$$

where Δ_0 is the low-energy thermodynamic scale and $\beta = 1/k_B T$. Similarly, for $P(t)$ we have at zero temperature $P(t) = \cos(\Omega_0 t)$ with $\Omega_0 = \Delta_0$ being the frequency of tunneling oscillations, which for this special case of $\alpha = 0$ coincides with the thermodynamic scale Δ_0. At finite α ($U < \infty$), the frictional effects of the environment renormalize both the dynamic scale $\Omega_0 \to \Omega_r(\alpha)$ and the thermodynamic scale $\Delta_0 \to \Delta_r(\alpha)$, such that they bifurcate from their common value at $\alpha = 0$, and an additional decay (or relaxation) time scale $1/\gamma_r(\alpha)$ enters the time-dependent dynamics [20]. In general, we shall define the thermodynamic scale at finite α, by $T_0 \equiv \Delta_r(\alpha) = 1/2\chi(0)$, so that it coincides with Δ_0 at $\alpha = 0$. This scale can also be considered as the relevant low-temperature Kondo scale since the charge susceptibility in the IRLM corresponds to the spin susceptibility in the equivalent AKM. While $\Omega_r(\alpha)$ is expected to vanish at $\alpha = \frac{1}{2}$, signaling a crossover to incoherent dynamics at $\alpha > \frac{1}{2}$ [20], the renormalized tunneling amplitude Δ_r vanishes only at $\alpha = 1^-$, with quantum mechanical tunneling absent at $\alpha > 1$ [i.e., $\Delta_r(\alpha > 1) = 0$]. At $\alpha = 1$, there is a quantum critical point with a phase transition of the Kosterlitz-Thouless type {in the IRLM, this occurs at $U = U^* = -(2/\pi\rho)\tan[\pi(\sqrt{2}-1)/2] \approx -0.969$}, which has been established by using the equivalence of the Ohmic two-state system to the AKM [2,67]. The Anderson-Yuval scaling equations for the latter [68] also yield an estimate for the renormalized tunneling amplitude Δ_r at finite α, namely, $\Delta_r(\alpha)/\omega_c = (\Delta_0/\omega_c)^{1/(1-\alpha)}$. Note that the latter result begins to differ from the exact low-energy scale $T_0(\alpha)$ for $\alpha \gtrsim \frac{1}{2}$ [69] (see also Fig. 1 in Sec. IV A).

III. METHODS

A. NRG and TDNRG

We briefly outline the NRG [70] and TDNRG [24] approaches and refer the reader to Refs. [24,26,71,72], respectively, for further details. The starting point to treat the IRLM in Eq. (2) with the NRG is a separation of the many energy scales in the conduction band via a logarithmic discretization $\epsilon_k = \pm D, \pm D\Lambda^{-(1-z)}, \pm D\Lambda^{-(2-z)}, \ldots$. Following Oliveira *et al.* [73], we have introduced a parameter z. Averaging physical quantities over several realizations of the band, defined by the parameter z, eliminates oscillations due to the logarithmic discretization of the band. These artificial oscillations are particularly evident in physical quantities calculated at large $\Lambda \gg 1$. In addition, this z-averaging procedure also proves useful in reducing artifacts in the time-dependent TDNRG results. Applying the Lanczos procedure with starting state defined by the local Wannier orbital $f_0 = \sum_k c_k$ to generate a new tridiagonal basis f_n, $n = 0,1,\ldots,$ for H_c results in the linear chain form

$$H_{\mathrm{IRLM}} = \varepsilon_d n_d + V(f_0^+ d + d^+ f_0) + U(n_d - 1/2)(n_0 - 1/2) + \sum_{n=0}^{\infty}\epsilon_n f_n^+ f_n + \sum_{n=0}^{\infty} t_n (f_n^+ f_{n+1} + f_{n+1}^+ f_n),$$

where the hoppings t_n decay exponentially along the chain (as $t_n \sim \Lambda^{-(n-1)/2}$, for $n \gg 1$), and, the onsite energies ϵ_n, which are in general finite, are zero for the particle-hole symmetric bands that we shall consider in this paper. Truncating the Hamiltonian H_{IRLM} to the first $m+1$ conduction orbitals $n = 0,1,\ldots,m$ and denoting this by H_m, we have the following recursion relation for the H_m:

$$H_{m+1} = H_m + \epsilon_{m+1} f_{m+1}^\dagger f_{m+1} + t_m (f_m^+ f_{m+1} + f_{m+1}^+ f_m).$$

By using this recursion relation, we can iteratively diagonalize the sequence of Hamiltonians H_m, $m = 0,1,\ldots,$ up to a maximum chain length $m = N$. The Hilbert space grows by a factor of 2 at each stage since each orbital f_n can be either empty or occupied. Truncation to the lowest N_{kept} states is required when $m > m_0$, where $m_0 \approx 10$ for $N_{\mathrm{kept}} = 1000$ states. We use electron number conservation in the diagonalization procedure and choose the maximum chain length in thermodynamic calculations such that the smallest scale in H_N, given approximately by $T_N = \Lambda^{-(N-1)/2}$, is smaller than $10^{-3}T_0$ with $T_0 = 1/2\chi(0)$ as defined earlier. This allows thermodynamics to be calculated at all temperatures of interest, i.e., for $10^{-3}T_0 \leqslant T \leqslant 2D$ where $2D = 2$ is the bandwidth (in practice we also ensure that $10^3 T_0 \ll 2D$ so that a part of the universal high-temperature asymptotic behavior in the temperature range $D \gg 10^3 T_0 \gg T \gg T_0$ is also captured, see Sec. IV A for details of how this is achieved). We average thermodynamic quantities, calculated by the conventional approach [33,71,74], over several z values, specified by $z_i = (2i-1)/2n_z$, $i = 1,n_z$, and use $n_z = 8$ and $\Lambda = 4$. The thermodynamic quantities of interest are the impurity contributions in which the host contribution is subtracted out. Thus, for the specific heat we have $C_{\mathrm{imp}}(T) = C_{\mathrm{tot}}(T) - C_0(T)$ where $C_{\mathrm{tot}}(T) = k_B\beta^2\langle(H_{\mathrm{IRLM}} - \langle H_{\mathrm{IRLM}}\rangle)^2\rangle$ and $C_0(T) = k_B\beta^2\langle(H_{\mathrm{bath}} - \langle H_{\mathrm{bath}}\rangle)^2\rangle$ are the specific heats of the total system and that of the host, respectively. Similarly, for the susceptibility, $\chi_{\mathrm{imp}}(T)$, we have $\chi_{\mathrm{imp}}(T) = \chi_{\mathrm{tot}}(T) - \chi_0(T)$, where $\chi_{\mathrm{tot}}(T) = \beta\langle(\hat{N} - \langle\hat{N}\rangle)^2\rangle$ and $\chi_0(T) = \beta\langle(\hat{N}_0 - \langle\hat{N}_0\rangle)^2\rangle$ are the charge susceptibilities of the total system and that of the host, respectively, and $\hat{N}$ and $\hat{N}_0$ the corresponding total electron number operators. The low-energy Kondo scale $T_0 = 1/2\chi(T=0)$ is extracted as in Eq. (3) from the local susceptibility $\chi(T) = -\partial n_d/\partial\varepsilon_d|_{\varepsilon_d\to 0}$. Note also that it is well known from the equivalence between the IRLM and the AKM that the two susceptibilities $\chi(T)$ and $\chi_{\mathrm{imp}}(T)$ differ only by a factor α, i.e., $\chi_{\mathrm{imp}}(T) = \alpha\chi(T)$ [22,23]. Thus, while we calculate $\chi_{\mathrm{imp}}(T)$, we shall show results for $\chi_{\mathrm{imp}}(T)/\chi_{\mathrm{imp}}(0)$ which are equal to the susceptibility of interest in the Ohmic two-state system $\chi(T)/\chi(0)$.

In TDNRG, we are interested in the dynamics of a local observable $\hat{O}$ following a quantum quench in which one or more system parameters of $H = H_{\mathrm{IRLM}}$ change suddenly at $t = 0$. Thus, the time dependence of H is described by $H(t) = \theta(-t)H^i + \theta(t)H^f$, with H^i and H^f being

time-independent initial- ($t < 0$) and final-state ($t > 0$) Hamiltonians, respectively [75]. The time evolution of $\hat{O}$ at $t > 0$ is then given by $O(t) = \mathrm{Tr}[\rho(t)\hat{O}]$ where $\rho(t) = e^{-iH^f t}\rho\, e^{iH^f t}$ is the time-evolved density matrix and $\rho = e^{-\beta H^i}/\mathrm{Tr}[\rho]$ is the equilibrium density matrix of the initial state at inverse temperature β. As shown in Ref. [24], $O(t)$ can be evaluated by making use of the complete basis set of discarded states to give

$$O(t) = \sum_{m=m_0}^{N} \sum_{rs \notin KK'} \rho_{sr}^{i\to f}(m) e^{-i(E_s^m - E_r^m)t} O_{rs}^m, \tag{5}$$

in which r and s may not both be kept states, $O_{rs}^m = {}_f\langle lem|\hat{O}|rem\rangle_f$ are the final-state matrix elements of $\hat{O}$, which are independent of the environment variable e labeling the complete set of discarded states $|lem\rangle$ (see Ref. [25] for details). In deriving the above, use has been made of the NRG approximation

$$H^f|rem\rangle \approx H_m^f|rem\rangle = E_r^m|rem\rangle, \tag{6}$$

and $\rho_{sr}^{i\to f}(m) = \sum_e {}_f\langle sem|\rho|rem\rangle_f$ represents the reduced density matrix of the initial state projected onto the basis of final states and termed the *projected density matrix*. The latter has been evaluated for the special choice of a density matrix defined on the longest Wilson chain

$$\rho = \sum_l |lN\rangle_i \frac{e^{-\beta E_l^N}}{Z_N} {}_i\langle lN|, \tag{7}$$

with $Z_N = \sum_l e^{-\beta E_l^N}$, in which only the discarded states of the last NRG iteration enter [24,25]. More recently, the projected density matrix has been evaluated for a general initial density matrix, given by the full density matrix [76,77] of the initial state, in Refs. [26,27]. This approach allows calculations to be carried out at zero or arbitrary temperature and is the approach that we use to obtain the results in this paper. It can be shown that the TDNRG is exact in the short-time limit, in the sense that $O(t \to 0^+)$ recovers the exact thermodynamic value $O^i = \mathrm{Tr}[\rho O]$ in the initial state [26]. The TDNRG remains stable and can be used to simulate to infinite times, however, the long-time limit of observables suffers from an error of typically a few % [25,26]. For the quantity of interest to us in this paper, $P(t)$, the absolute error in $P(t \to \infty)$ varies from approximately 10^{-6} at $\alpha = 0.001 \ll 1$ to approximately 0.07 at $\alpha = 0.9$ (see Table II). In addition to this error, TDNRG exhibits "noise" at long times $t \gtrsim 1/\gamma_r(\alpha)$, where, for the IRLM, $1/\gamma_r(\alpha)$ is the relaxation time defining the decay of $P(t)$. This noise can be significantly reduced by the z-averaging procedure, with typically $n_z = 32$ [25,26]. Note that the use of z averaging here is different to its use in thermodynamic calculations. In the latter, the aim is not to eliminate noise, but to eliminate discretization induced oscillations in physical quantities which occur when using a large Λ. We do not use any damping for the time-dependent factors $e^{-i(E_s^m - E_r^m)t}$ entering Eq. (5).

For the calculations of $P(t)$ in this paper, we used the following quench protocol. The initial-state Hamiltonian H_i is given by the IRLM with finite hybridization $V_i = V$, a fixed Coulomb interaction $U_i = U$, and a local level $\varepsilon_{d,i}/\Gamma \ll -1$ such that the level is singly occupied. This corresponds to an initial-state preparation of the Ohmic two-state system in the state $\sigma_z = 2(n_d - 1/2) = +1$, with the oscillators relaxed with respect to this state of the two-level system. The final-state Hamiltonian H_f is again given the IRLM with the same $V_f = V_i = V$ and $U_f = U_i = U$ as for H_i, but with level position $\varepsilon_{d,f} = 0$ corresponding to an unbiased Ohmic two-state. This protocol is used also in the TD-DMRG and FRG calculations. As we wish to compare with these methods, we shall also restrict our TDNRG calculations for $P(t)$ to zero temperature.

B. DMRG and TD-DMRG

We use the numerically exact DMRG scheme formulated in matrix product states (MPS) to benchmark the results obtained within NRG at arbitrary spin-boson coupling α (or U in the language of the IRLM). A detailed introduction to the DMRG using MPS can be found in one of the many good reviews (e.g., Refs. [78,79]). Using MPS means that we rewrite any quantum state via

$$\begin{aligned}|\Psi\rangle &= \sum_{n_1,\ldots,n_N} c_{n_1,\ldots,n_L}|n_1,\ldots,n_N\rangle \\ &= \sum_{n_1,\ldots,n_N} A^{n_1},\ldots,A^{n_L}|n_1,\ldots,n_N\rangle\end{aligned} \tag{8}$$

as a product of (local) matrices A^{n_i}, where n_i is the local degree of freedom (such as the occupancy of the ith site). Such a decomposition is always possible, but the size of the matrices A grows exponentially in system size. Fortunately, one can usually capture all relevant physics approximating the matrices A by a singular value decomposition and keeping only the most relevant singular values. The square of the singular values discarded is denoted by χ in the following and we always choose $\chi \approx 10^{-7}\ldots 10^{-9}$ such that the numerics are converged with respect to this numerical parameter. By this procedure, numerically exact results are obtained while maintaining feasible sizes for the matrices A.

For non-translation-invariant systems DMRG can be applied to a finite system only and thus to address the IRLM we use a lead of finite length L. The total size of the system (reservoir plus dot) is thus $N = L + 1$. By performing separate calculations for different L, we verified that the considered L are large enough such that finite-size effects can be disregarded (for the time scales considered). It is important to stop the calculation before recurrence effects (information of the end of the chain has traveled through the lead to the dot) set in. Furthermore, for simplicity we concentrate on a semielliptic density of states in the reservoir leading to

$$\begin{aligned}H_{\mathrm{IRLM}} = \varepsilon_d n_d + V(f_0^+ d + d^+ f_0) + U(n_d - 1/2)(n_0 - 1/2) \\ + D/2\sum_{n=0}^{L-1}(f_n^+ f_{n+1} + f_{n+1}^+ f_n),\end{aligned}$$

which is convenient for standard DMRG implementations as only nearest-neighbor terms have to be treated. Here, the bandwidth is $2D$. We concentrate on the same quench protocol as described in the previous section III A. To address the dynamics, we use a two-site version of an iterative ground-state algorithm (to find the initial state) as well as a symmetric fourth-order Suzuki-Trotter decomposition for the

(subsequent) time evolution, as described in Chaps. 6 and 7 of Ref. [79], respectively.

The main idea of the iterative ground-state algorithm is to start from some initial occupancy configuration of fermions in the lead plus dot space and then repetitively sweep through the chain from left to right and right to left, optimizing the occupancy configuration of two sites at a time with respect to the total energy. For a sufficiently large number of sweeps, the energy converges and the ground state is achieved. During the sweeping process, the dimensions of the matrices A increase and thus have to be truncated using a singular value decomposition (as described above).

After preparing the ground state $|\Psi\rangle$, we perform a real-time evolution to obtain $|\Psi\rangle(t = n\tau)$ by applying n times a Trotter decomposed version of $e^{-iH\tau}$. To achieve this, we separate even and odd sites $H = \sum_{i\ \mathrm{odd}} h_i + \sum_{i\ \mathrm{even}} h_i$ and approximate $e^{-iH\tau} \approx U(\tau_1)U(\tau_2)U(\tau_3)U(\tau_2)U(\tau_1)$, where

$$U(\tau_j) = e^{-i\sum_{i\ \mathrm{odd}} h_i\tau_j/2} e^{-i\sum_{i\ \mathrm{even}} h_i\tau_j} e^{-i\sum_{i\ \mathrm{odd}} h_i\tau_j/2}, \quad (9)$$

$$\tau_1 = \tau_2 = \frac{1}{4 - 4^{1/3}}\tau, \quad \tau_3 = \tau - 2\tau_1 - 2\tau_2. \quad (10)$$

Decreasing τ (increasing n) systematically improves on the accuracy of the Trotter decomposition. During the time evolution, the dimensions of the matrices A increase and the need for approximating them via the singular value decomposition and disregarding the smallest singular values arises. This is done efficiently after each applied $U(\tau_j)$. Eventually, at given χ the dimensions of the matrices A increase beyond the numerically feasible level and the simulation has to be stopped.

For each plot we checked that the numerical parameters were chosen such that further increasing the accuracy of the DMRG does not alter the curves (on the scales shown). As we have to perform a time evolution using a Trotter decomposition, we cannot access the deep scaling limit of the IRLM, simply because decreasing V/D requires to resolve larger times t (and consequently a larger number of time steps n and also larger reservoir size L to avoid recurrence). Thus, eventually when decreasing V/D, one fails to perform the numerical calculation due to resource limitations. Nevertheless, in the following, values of V/D as small as $V/D \approx 0.1$ can easily be addressed.

C. FRG

In addition to the NRG and DMRG, we use the FRG approach to determine the time evolution of the IRLM. Within the FRG a truly infinite system can be tackled by using standard projection techniques [80]. With this the influence of the infinite noninteracting reservoir onto the dot system is incorporated exactly. Later, we will treat some of the reservoir degrees of freedom explicitly and only project out the rest, to efficiently model different reservoir density of states. Therefore, in the following we do not focus on a single level, but an extended interacting dot geometry coupled to (structureless) reservoirs. Again, we only summarize the main ideas as well as extensions needed and refer the reader to Ref. [62] for additional technical details. We employ the framework of the Keldysh Green's functions G to derive an exact infinite hierarchy of flow equations of the form

$$\partial_\Lambda \gamma_m^\Lambda = f_m\big(G^\Lambda, \gamma_{m+1}^\Lambda, \gamma_m^\Lambda, \gamma_{m-1}^\Lambda, \dots\big), \quad (11)$$

where γ_m are the irreducible vertex functions.

The Λ dependency is introduced by an auxiliary cutoff in the noninteracting Green function

$$G_0 \to G_0^\Lambda, \quad G^{\Lambda\to\infty} = 0, \quad G_0^{\Lambda\to 0} = G_0, \quad (12)$$

which leads to a successive incorporation of energy degrees of freedom from high to low. We concentrate on the so-called hybridization cutoff, which consists in coupling one additional reservoir with infinite temperature to each level of the (extended) quantum dot. Each of these auxiliary reservoirs couples to the corresponding dot level via a hybridization Λ. Starting at $\Lambda \to \infty$, where all degrees of freedom are cut out ($G^{\Lambda\to\infty} = 0$), we integrate to $\Lambda = 0$, where the artificial cutoff is removed and the physical situation is restored. The infinite hierarchy of flow equation, being an exact reformulation of the quantum many-body problem, can not be solved in its entity. Thus, one needs to truncate it to a certain order. Here, we employ the first-order truncation scheme. In turn, the results are controlled up to leading order in the interaction U, but contain power-law resummations superior to a plain perturbative approach. Within this lowest-order truncation scheme, the flow of the Keldysh self-energy vanishes and we need to determine the retarded self-energy contribution only. As a consequence, the interacting system can be interpreted as a noninteracting one with renormalized time-dependent parameters. For the IRLM, the corresponding flow equation takes the form

$$\partial_\Lambda \Sigma_{kl}^{\mathrm{ret}}(t',t) = -i \sum_{ijkl} \frac{U_{ijkl}(t)}{2} \delta(t'-t) S_{lj}^{\mathrm{K}}(t,t) \quad (13)$$

with

$$S^{\mathrm{K}} = -iG^{\mathrm{ret}}G^{\mathrm{K}} + iG^{\mathrm{K}}G^{\mathrm{adv}} \quad (14)$$

for the used infinite-temperature hybridization cutoff. U_{ijkl} denotes the antisymmetrized two-particle interaction, where the indices label single-particle levels. Equation (14) involves the real-time representation of the Dyson equations

$$G^{\mathrm{ret}}(t,t') = G^{0,\mathrm{ret}}(t,t') + [G^{\mathrm{ret}}\Sigma^{\mathrm{ret}}G^{0,\mathrm{ret}}](t,t'), \quad (15)$$

$$G^{\mathrm{K}}(t,t') = -iG^{\mathrm{ret}}(t,0)(1-2\bar{n})G^{\mathrm{adv}}(0,t') + \big[G^{\mathrm{ret}}\big(\Sigma_{\mathrm{lead}}^{\mathrm{K}} + \Sigma^{\mathrm{K}}\big)G^{\mathrm{adv}}\big](t,t'). \quad (16)$$

One can now employ the ideas of Ref. [62] to solve these in a very efficient and numerically exact fashion. To solve the remaining differential flow equation (13), we employ a standard Runge-Kutta procedure. The relative and absolute tolerance of this Runge-Kutta integrator were chosen to be 10^{-6} and 10^{-8}, respectively. An advantage of the FRG compared to the TDNRG or TD-DMRG methods used in this paper is that results can be obtained with far less computational effort. Observables, such as the occupancy and thus $P(t)$, can be deduced from the Green's functions via

$$\bar{n}_i(t) = \frac{1}{2} - \frac{i}{2} G_{ii}^{\mathrm{K}}(t,t). \quad (17)$$

This concludes our short and general summary of the FRG approach to transient dynamics.

Within the approach described in Ref. [62] one can only capture reservoirs in the scaling limit. To make contact with the NRG and DMRG, we extend the formalism of Ref. [62] to reservoirs with an arbitrary density of states. To achieve this, we keep an increasing number of reservoir sites explicit in our calculation, effectively treating them as part of the dot structure. For the sites kept explicitly we use a linear geometry, where the one end couples to the dot and the other end couples to a structureless reservoir modeling all additional reservoir sites. The hopping within the explicitly treated part of the reservoir can then be chosen such that the local density of states of the only site connected to the dot has the desired form. As this boundary density of states is the only relevant quantity for any local dot observable, this method becomes numerically exact upon increasing the explicitly treated reservoir sites (and with them the number of optimization parameters to fit the density of states). In practice, we find that approximately only 20 sites suffice to converge this process.

IV. RESULTS

A. Thermodynamics

For the thermodynamics of the Ohmic two-state system, we are primarily interested in universal results for specific heats and susceptibilities in the temperature range $10^{-3}T_0 \leqslant T \leqslant 10^3 T_0 \ll D$ with T_0 chosen sufficiently small so that nonuniversal effects coming from the finite bandwidth $2D = 2$ are minimized. For given α (corresponding to a given U in the IRLM), this requires choosing V in the IRLM sufficiently small in order that the highest temperatures of interest $T_{\max} = 10^3 T_0$ are still much smaller than the half-bandwidth D, i.e., $T_{\max} \ll D$. Since T_0 is *a priori* unknown, this poses the problem of how to choose an appropriate hybridization $V = \Delta_0/2$ for a given α. We proceeded as follows: set $T_0(\alpha) \approx \Delta_{\rm eff}(\alpha) = 10^{-10}$ and solve for V. The scale $\Delta_{\rm eff}(\alpha)$ is related to the scaling result for the renormalized tunneling amplitude of the Ohmic two-state system $\Delta_{\rm r}(\alpha) = \omega_c(\Delta_0/\omega_c)^{1/(1-\alpha)}$ via [20]

$$\Delta_{\rm eff}(\alpha) = [\Gamma(1-2\alpha)\cos(\pi\alpha)]^{1/2(1-\alpha)}\Delta_{\rm r}(\alpha), \qquad (18)$$

where Γ is the Γ function. If need be, a smaller $\Delta_{\rm eff}(\alpha) < 10^{-10}$ can be chosen, but this was not necessary for $\alpha \leqslant 0.9$. We could also have estimated a value for V by setting $T_0 \approx \Delta_{\rm r}(\alpha) = 10^{-10}$, however, the latter scale deviates considerably more from $T_0(\alpha)$ than $\Delta_{\rm eff}(\alpha)$ in the regime $\alpha > \frac{1}{2}$, being considerably smaller, and hence would have resulted in unnecessarily small values of V. This is illustrated in Fig. 1, which shows the α dependence of $T_0(\alpha)$ and compares it to that of $\Delta_{\rm eff}(\alpha)$ and $\Delta_{\rm r}(\alpha)$ for a fixed V and constant density of states (see also Table II for numerical values).[3] Note that the adiabatic renormalization result for the low-energy scale

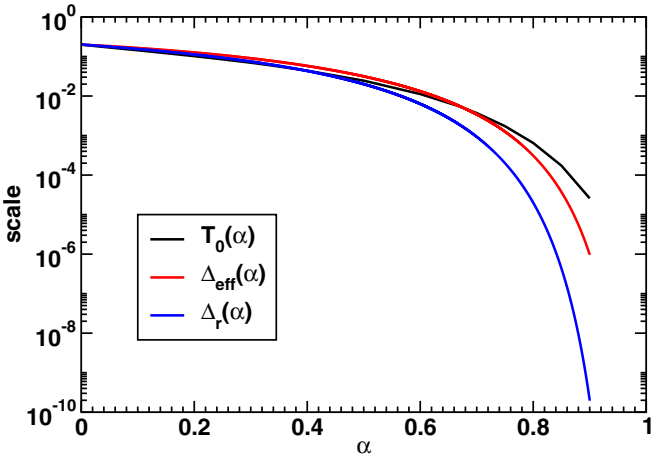

FIG. 1. The susceptibility scale $T_0(\alpha) = 1/2\chi(0)$ vs α for the IRLM using $V = 0.1D$ and a constant density of states $\rho(\omega) = 1/2D$ with $D = 1$. Also shown are $\Delta_{\rm eff}(\alpha)$, and $\Delta_{\rm r}(\alpha)$ vs α. NRG parameters used to calculate $T_0(\alpha)$: $\Lambda = 4$, $n_z = 8$, and $N_{\rm kept} = 1000$.

$\Delta_{\rm r}(\alpha)$ is close to the correct scale $T_0(\alpha)$ only for $\alpha \lesssim \frac{1}{2}$. We have also checked that our calculation of $T_0(\alpha)$ agrees with similar NRG calculations in Ref. [52].

1. Specific heat

We show in Fig. 2 the evolution of the specific-heat curves of the Ohmic two-state system (calculated via the IRLM) as a function of temperature for increasing dissipation

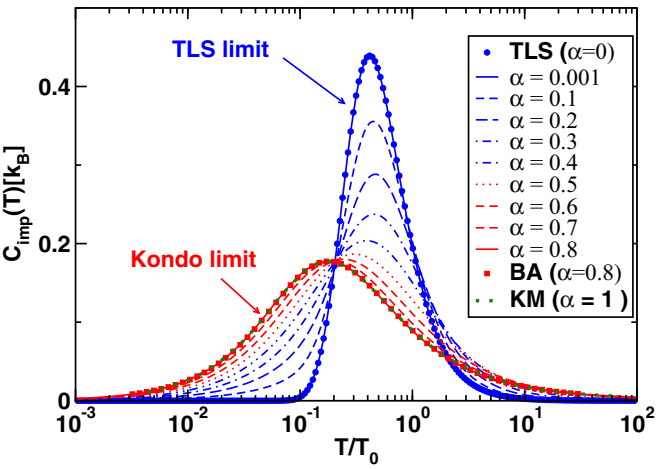

FIG. 2. Evolution of the impurity contribution to the specific heat $C_{\rm imp}$ with increasing dissipation strength α, from weak ($\alpha < \frac{1}{2}$) to strong ($\alpha > \frac{1}{2}$) dissipation. Lines: results for the Ohmic two-state system obtained via the IRLM using NRG. Also shown (symbols) are the isolated two-level system result ($\alpha = 0$) using Eq. (4) and the Bethe ansatz result (via the AKM) for $\alpha = \frac{4}{5}$ [23]. KM: the universal specific-heat curve for the isotropic Kondo model ($\alpha \to 1^-$) with its T_0 adjusted so that this curve coincides with the $\alpha = 0.8$ curve (this adjustment of T_0 is done in order to show that the $\alpha = 0.8$ curve, while still not identical to the isotropic Kondo model curve, nevertheless lies very close to it; without such an adjustment, the isotropic Kondo model curve would lie slightly to the left) (from Ref. [81]). NRG parameters as in Fig. 1.

[3] We do not imply that $\Delta_{\rm eff}(\alpha)$ should be equal to the thermodynamic scale T_0. In fact, $\Delta_{\rm eff}(\alpha)$ is a scale that enters in the transient dynamics (see Sec. IV B 1 and Ref. [20]). Our use of $\Delta_{\rm eff}(\alpha)$ in the context of this section is only as a means to obtain a rough estimate for an input V for our NRG calculations.

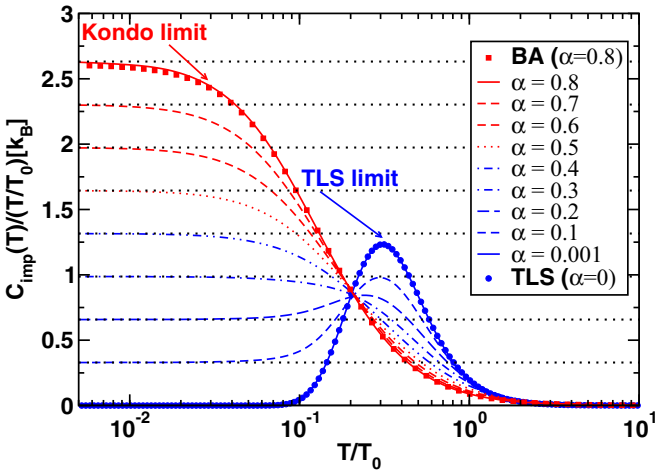

FIG. 3. $C_{\rm imp}/(T/T_0)$ vs T/T_0 for increasing dissipation strength α as in Fig. 2. Horizontal dotted lines indicate the exact Fermi liquid value at $T=0$, given by $\pi^2\alpha/3$ [23]. Lines: results for the Ohmic two-state system obtained via the IRLM using NRG. Also shown (symbols) are the isolated two-level system result ($\alpha=0$) using Eq. (4) and the Bethe ansatz result (via the AKM) for $\alpha=\frac{4}{5}$ [23]. NRG parameters as in Fig. 1.

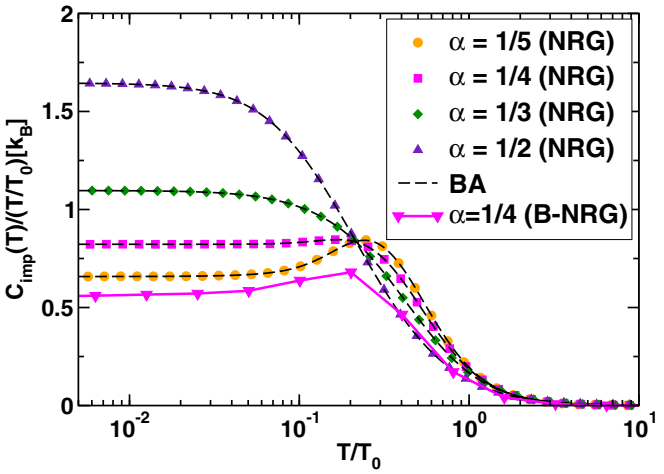

FIG. 4. $C_{\rm imp}(T)/(T/T_0)$ vs T/T_0 for the IRLM for $\alpha=\frac{1}{5}$, $\frac{1}{4}$, $\frac{1}{3}$, $\frac{1}{2}$ (symbols) compared to corresponding Bethe ansatz calculations (dashed lines) [23]. NRG parameters as in Fig. 1. For comparison, we also show the $\alpha=\frac{1}{4}$ result (B-NRG) calculated from the bosonic NRG [45].

strengths ranging from very weak dissipation ($\alpha \ll 1$) to strong dissipation strengths ($\alpha > \frac{1}{2}$). The peak position in the specific heat shifts from $T_{\rm p} \approx 0.42T_0$ at $\alpha \ll 1$ to $T_{\rm p} \approx 0.17T_0$ at $\alpha = 0.8$. Note the approximate crossing point at $T \approx 0.2T_0$, a characteristic feature in many correlated systems [82]. We also show the curve for the isolated two-level system ($\alpha=0$) from Eq. (4). Although this appears to fit the $\alpha=0.001$ curve at all temperatures, the latter, in contrast to the former, exhibits Fermi liquid behavior at low temperatures due to the gapless nature of the excitations in the Ohmic two-state system. The deviations between the cases $\alpha=0$ and $\alpha \ll 1$ will be discussed in more detail below. We have also compared the specific heat at $\alpha=0.8$ with that for the AKM from the numerical solution of the thermodynamic Bethe ansatz equations of the latter [23,32], finding good agreement at all temperatures. Indeed, the numerical results for $C_{\rm imp}(T)$ at asymptotically high ($T \gg T_0$) and low ($T \ll T_0$) temperatures obtained from the IRLM agree with those extracted from the Bethe ansatz for the equivalent AKM for all finite α:[4]

$$C_{\rm imp}(T \gg T_0)/k_{\rm B} \approx a\left(\frac{T_0}{T}\right)^{\nu_c}, \tag{19}$$

$$C_{\rm imp}(T \ll T_0)/k_{\rm B} \approx \frac{\pi^2\alpha}{3}\frac{T}{T_0}, \tag{20}$$

with $\nu_c = 2-2\alpha$ and the constant a depending only on α. The above asymptotic behavior is also recovered in path-integral approaches [20,29,83]. We can test the accuracy of the Fermi liquid result by plotting $C_{\rm imp}(T)/(T/T_0)$ vs T/T_0 as in Fig. 3. One sees that the result (20) is recovered for all finite α in the limit $T/T_0 \ll 1$ (dotted lines). Furthermore, one notices for the case $\alpha=0.8$ that the numerical result from the IRLM is more accurate than that from the numerical solution of the TBA equations since the latter yield a value for $\lim_{T\to 0} C_{\rm imp}(T)/(T/T_0)$ which differs from the exact Fermi liquid result in Eq. (20) by 1%. In contrast, the IRLM result is accurate to within 0.1% in this limit. We emphasize that for general α, Bethe ansatz results are not readily available due to the complexity of the TBA equations, whereas NRG calculations for the IRLM can be carried out for any α and are seen to be highly accurate. In Fig. 4, we compare results for $C_{\rm imp}(T)/(T/T_0)$ obtained via the IRLM at weak dissipation $\alpha \leqslant \frac{1}{2}$ with available Bethe ansatz results for the AKM, finding also here excellent agreement between these results. We also show data for $C_{\rm imp}(T)/(T/T_0)$ at $\alpha=\frac{1}{4}$ obtained within the bosonic NRG approach to the Ohmic spin-boson model [45]. The latter cannot be brought into correspondence with our IRLM curve for $\alpha=\frac{1}{4}$ since the finite-temperature peak in the bosonic NRG is too large.[5] Thermodynamic properties probe all excitations of the system and might be the most difficult properties to capture quantitatively in the bosonic NRG [45]. Increasing the number of states and performing more refined calculations using a larger Λ to reduce truncation errors while implementing z averaging might reduce the difference between these early bosonic NRG studies of the specific heat and that calculated within the IRLM in this paper. While the trends with α in $C(T)/T$ within bosonic NRG are qualitatively the same as in the IRLM [in particular, bosonic NRG also describes the appearance of a finite-temperature peak in $C(T)/T$ for $\alpha \lesssim \frac{1}{3}$, see Ref. [45]], at present quantitative differences exist.

We now return to discussing the aforementioned differences between the specific heat of a weakly interacting Ohmic two-state system (i.e., $\alpha \ll 1$) and that of an isolated two-level

[4]Note that the thermodynamic scale in Ref. [23] denoted there by $\Delta_{\rm r}$ is related to our present definition via $\Delta_{\rm r} = \pi T_0$.

[5]We have adjusted the scale $T^* \sim T_0$ [45] by a factor 2 so that the high-temperature asymptotes approximately match in the comparison.

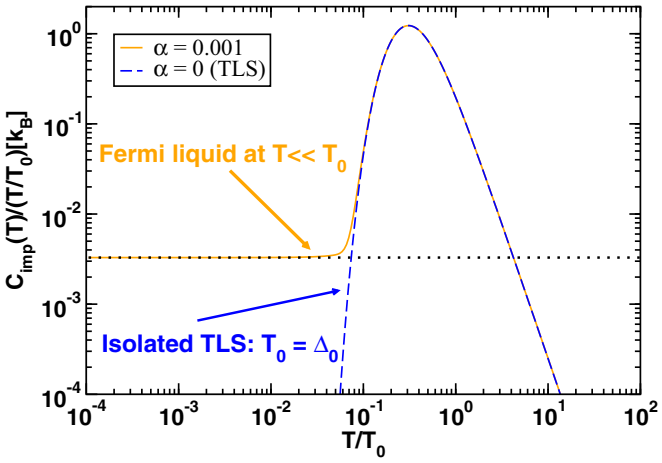

FIG. 5. Specific heat divided by temperature $C_{\rm imp}(T)/(T/T_0)$ vs T/T_0 of a weakly coupled Ohmic two-state system ($\alpha = 0.001 \ll 1$) compared to that of an isolated two-level system ($\alpha = 0$). The former exhibits Fermi liquid behavior at $T \ll T_0$, and activated behavior in the range $0.1T_0 \lesssim T \lesssim 0.3T_0$, while the latter, having a gapped spectrum with $T_0 = \Delta_0$, exhibits activated behavior for all $T \lesssim 0.3T_0$. Dotted line: Fermi liquid result from Eq. (20). NRG parameters as in Fig. 1.

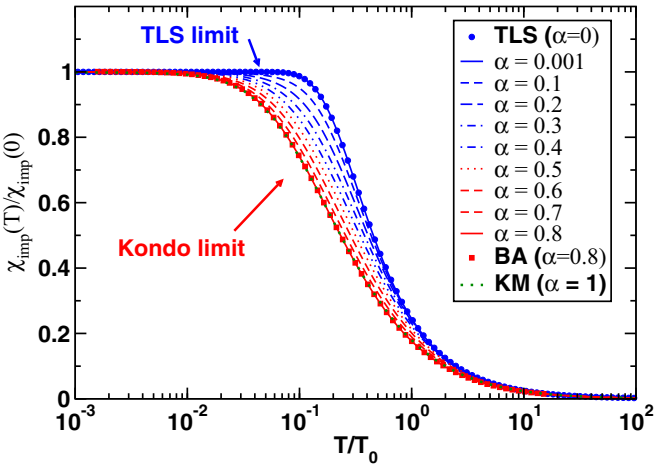

FIG. 6. Impurity contribution to the charge susceptibility $\chi_{\rm imp}(T)$ normalized to its $T = 0$ value vs T/T_0 for increasing dissipation strength α, from weak ($\alpha < \frac{1}{2}$) to strong ($\alpha > \frac{1}{2}$) dissipation. Lines: results for the Ohmic two-state system obtained via the IRLM. Also shown (symbols) are the isolated two-level system result ($\alpha = 0$) using Eq. (3) and the Bethe ansatz result for $\alpha = \frac{4}{5}$ (via the equivalence to the AKM [23]). KM: the universal susceptibility heat curve for the isotropic Kondo model ($\alpha \to 1^-$) with T_0 adjusted to coincide with that for $\alpha = 0.8$ (from Ref. [85]). NRG parameters as in Fig. 1.

system (i.e., $\alpha = 0$). In Fig. 5, we show on a log-log plot the comparison for $C_{\rm imp}(T)/(T/T_0)$ vs T/T_0. Depicted in this way, it is evident that the isolated two-level system provides a good description of the specific heat of a weakly interacting Ohmic two-state system only down to temperatures of order $0.1T_0$. Below this temperature (i.e., for $T \ll T_0$), clear differences appear, with the former exhibiting an activated behavior $C_{\rm imp(T)}(T)/(T/T_0) \approx k_{\rm B}(T_0/T)^3 \exp[-1/(T/T_0)]$, and the latter exhibiting the Fermi liquid behavior given by Eq. (20), i.e., $C_{\rm imp}(T)/(T/T_0) \approx k_{\rm B}\pi^2\alpha/3$ for $T \ll T_0$. The dotted line in Fig. 5 shows that the $T \to 0$ limit of this Fermi liquid result is indeed recovered even for this very weakly interacting ($\alpha = 0.001$) Ohmic two-state system.

We comment briefly on universality of physical quantities in the present context. Universal results, in the rigorous sense, are obtained by taking the limit $\Delta_0/\omega_c \to 0$ while maintaining a finite low-energy scale T_0. This scaling limit can be taken in analytic approaches and leads to a one-parameter family for physical quantities, such as specific heats $C_\alpha(T)$, which are functions of the reduced temperature $T/T_0(\alpha)$ and whose functional form is determined only by α (see [23,31,32]). Numerically, we always have a finite $\Delta_0/\omega_c = V/D$, resulting in nonuniversal corrections at high temperatures. These can, however, be shifted to arbitrarily high temperatures by choosing a sufficiently small V/D. From the equivalence of the Ohmic two-state system to the AKM, the limit $\alpha \to 1^-$, maintaining a finite T_0 while taking the limit $\Delta_0/\omega_c \to 0$ recovers the universal scaling functions for the isotropic Kondo model. In this limit, the specific heat $C(T) = C_{\alpha=1}(T)$ acquires logarithmic corrections at high temperatures instead of the power-law corrections (19) for $\alpha < 1$ [32]. In Fig. 2, we show for comparison the universal specific-heat curve of the isotropic Kondo model $C_{\alpha=1}$ [32,81,84] with Kondo scale adjusted to match $T_0(\alpha = 0.8)$. While the $C_{\alpha=0.8}$ curve is strictly different from the $C_{\alpha=1}$ curve at asymptotically high temperatures, we see that, for the temperature range shown, the two curves are very close.

2. Susceptibility

The temperature dependence of the normalized impurity susceptibility $\chi_{\rm imp}(T)/\chi_{\rm imp}(0)$ is shown in Fig. 6 for a range of dissipation strengths ranging from weak ($\alpha \ll 1$) to strong ($\alpha > \frac{1}{2}$) dissipation. As for the specific heats, we see also here how the susceptibility of the isolated two-level system, given by Eq. (3), smoothly evolves with increasing dissipation strength into the spin susceptibility of the (isotropic) Kondo model as $\alpha \to 1^-$. The equivalence of the IRLM to the AKM implies that the charge susceptibility $\chi_{\rm imp}$ of the former maps onto the spin susceptibility of the latter (since $n_d - 1/2$ in the IRLM maps onto S_z in the AKM). Indeed, we find that our numerical results for the IRLM at asymptotically low ($T \ll T_0$) and high ($T \gg T_0$) temperatures correspond to those of the AKM as extracted from the Bethe ansatz solution

$$\chi_{\rm imp}(T \gg T_0) \approx \frac{\chi_{\rm imp}(0)}{4}\frac{T_0}{T}\left[1 - 4b\left(\frac{T_0}{T}\right)^{\nu_\chi}\right], \qquad (21)$$

$$\chi_{\rm imp}(T \ll T_0) \approx \chi_{\rm imp}(0)\left[1 - c\left(\frac{T}{T_0}\right)^2\right], \qquad (22)$$

with $\nu_\chi = \nu_c = 2 - 2\alpha$ and constants b,c depending only on α (see Table I and Fig. 15).

3. Wilson ratio

We can define a Wilson ratio for the Ohmic two-state system in terms of $\chi(T) = \chi_{\rm imp}(T)/\alpha$ and $C_{\rm imp}(T)$ via $R_{\rm sb} = \lim_{T\to 0} 4\pi^2\chi(T)/3C_{\rm imp}(T)/T$ in analogy to the definition of this quantity for the Kondo and Anderson models [86]. This yields, upon using Eqs. (20) and (22), the value $2/\alpha$.

TABLE I. Numerical estimates of ν_c and ν_χ entering the high-temperature specific heat and susceptibilities in Eqs. (19) and (21). Wilson ratio $R_{\rm AKM}$.

α	ν_c	ν_χ	$R_{\rm AKM}$
0.001	2.00	2.03	2.00017
0.1	1.79	1.78	2.0002
0.2	1.59	1.61	2.0019
0.3	1.39	1.39	2.00079
0.4	1.20	1.20	2.00018
0.5	1.00	0.99	2.00002
0.6	0.80	0.80	2.00009
0.7	0.61	0. 61	2.0002
0.8	0.45[a]	0.41	2.0025

[a]The stronger deviation from the expected value $2-2\alpha=0.4$ for this case indicates that V/D needs to be reduced further in order to access the leading high-temperature correction.

Note that this equals the known value of 2 in the isotropic Kondo limit $\alpha\to 1^-$ when the susceptibilities $\chi(T)$ and $\chi_{\rm imp}$ become equal. Equivalently, one may define a Wilson ratio for the AKM, by using the relevant susceptibility for the latter $\chi_{\rm imp}$, i.e., $R_{\rm AKM}=\lim_{T\to 0}4\pi^2\chi_{\rm imp}(T)/3C_{\rm imp}(T)/T$. The latter is then exactly 2 for all α, i.e, for all anisotropies in the AKM [32]. This is demonstrated numerically in Fig. 7 where we show the temperature dependence of the quantity $4\pi^2\chi_{\rm imp}(T)/3C_{\rm imp}(T)/T$ for a range of dissipation strengths. The numerical values for $R_{\rm AKM}$ lie within 0.2% of the exact value for all α (see Table I). Note the different approach of $4\pi^2\chi_{\rm imp}(T)/3C_{\rm imp}(T)/T$ to the universal $T=0$ value of 2 upon decreasing temperature below T_0 for small- and large-α cases. The smallness of the above quantity in the range $0.1\leqslant T/T_0\leqslant 1$ at small $\alpha\lesssim 0.3$ is due to the appearance of a peak in $C_{\rm imp}(T)/T$ at weak dissipation, reflecting the onset of activatedlike behavior in this limit (see Fig. 3).

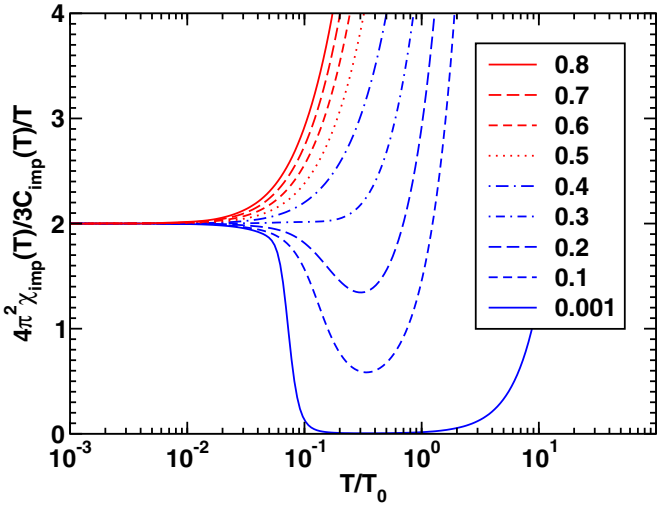

FIG. 7. $4\pi^2\chi_{\rm imp}(T)/3C_{\rm imp}(T)/T$ vs T/T_0. This tends to the Wilson ratio $R_{\rm AKM}=2$ in the limit $T\to 0$ for all α to an accuracy of less than 0.1%. The corresponding quantity for the Ohmic two-state system $4\pi^2\chi(T)/3C_{\rm imp}(T)/T$ with $\chi(T)=\chi_{\rm imp}(T)/\alpha$ yields a Wilson ratio of $2/\alpha$ in the limit $T\to 0$.

B. Transient dynamics

In this section, we present TDNRG results for $P(t)=\langle\sigma_z(t)\rangle$ of the symmetric Ohmic two-state system at short $[t\ll 1/\Delta_{\rm eff}(\alpha)]$ to intermediate $[t\sim 1/\Delta_{\rm eff}(\alpha)]$ time scales for the whole range of dissipation strengths $0<\alpha<1$ and compare these with results from the NIBA [2] (Sec. IV B 1), the TD-DMRG [79,87–90] (Sec. IV B 2), and the FRG [28,63,91] (Sec. IV B 3). The methods are complementary: TDNRG and TD-DMRG are nonperturbative in the dissipative coupling α and can be used to investigate the dynamics at both weak ($\alpha<\frac{1}{2}$) and strong dissipations ($\alpha>\frac{1}{2}$), while the regime of validity of the NIBA is generally believed to lie in the region $0\leqslant\alpha\lesssim\frac{1}{2}$ (and not too long times, see below). The FRG for the IRLM is, by construction, exact at $\alpha=\frac{1}{2}$ (corresponding to $U=0$ in the IRLM), and remains quantitatively accurate in a finite interval around $\alpha=\frac{1}{2}$, becoming inaccurate in the limits $\alpha\to 0$ (corresponding to $U\to\infty$ in the IRLM) and $\alpha\to 1^-$ (corresponding to $U\to U^*=-0.969$ in the IRLM). The comparisons below shed further light on the validity of the various approaches in different regimes and time ranges. The accuracy of the NIBA, for example, has not been convincingly tested against other reliable methods for general values of α, despite the considerable literature on the Ohmic two-state system, and recent results revise the picture of the crossover from coherent to incoherent dynamics [28,42] (see Sec. IV B 3 for a discussion of this).

1. Comparison with NIBA

For the purpose of comparing TDNRG results with NIBA results, it is useful to first briefly summarize the content of the NIBA for $P(t)$. At $T=0$, the NIBA provides the following analytic expression for $P(t)$ [2,20]:

$$P_{\rm NIBA}(t)=E_{2-2\alpha}\{-[\Delta_{\rm eff}(\alpha)t]^{2-2\alpha}\},\qquad(23)$$

where $E_\nu(z)$ is the Mittag-Leffler function and $\Delta_{\rm eff}(\alpha)$ is defined in Eq. (18). The NIBA is generally considered to be a reasonable approximation for the short time $[t\ll 1/\Delta_{\rm eff}(\alpha)]$ to intermediate time $[t\sim 1/\Delta_{\rm eff}(\alpha)]$ dynamics of the Ohmic two-state system in the regime $0\leqslant\alpha\leqslant\frac{1}{2}$ (being exact at $\alpha=0$ and at $\alpha=\frac{1}{2}$). Specifically, for $0\leqslant\alpha<\frac{1}{2}$, Eq. (23) predicts (for not too long times) coherent oscillations with frequency $\Omega_r(\alpha)=\cos[\pi\alpha/2(1-\alpha)]\Delta_{\rm eff}(\alpha)\theta(1/2-\alpha)$ and decay rate $\gamma_r(\alpha)=\sin[\pi\alpha/2(1-\alpha)]\Delta_{\rm eff}(\alpha)$. At $\alpha=\frac{1}{2}$, the NIBA result $P_{\rm NIBA}(t)=\exp(-2\Gamma t)$ is exact (in the scaling limit of the SBM). Here, $\Gamma=\pi(\Delta_0/\omega_c)^2\omega_c/4=\pi\rho V^2$ is the bare resonance level width of the equivalent IRLM, upon using $\Delta_0/\omega_c=V/D$, $\omega_c=2D$ (see Appendix A and Table III). While the NIBA is not justified in the regime $\frac{1}{2}<\alpha<1^-$ (see Refs. [2,20]), it is nevertheless instructive to show comparisons with the NIBA also in this regime. For $\alpha>\frac{1}{2}$, the NIBA predicts that the dynamics is incoherent, but with $P_{\rm NIBA}(t)$ incorrectly decaying algebraically instead of exponentially (see below for more details). At asymptotically short times $t\ll 1/\Delta_{\rm eff}(\alpha)$, NIBA yields the behavior $P_{\rm NIBA}[t\ll 1/\Delta_{\rm eff}(\alpha)]\approx 1-(\Delta_{\rm eff}(\alpha)t)^{2-2\alpha}/\Gamma(3-2\alpha)$ for all α [2,20]. Notice, however, that the ultrashort time scale $1/\omega_c$, associated with the cutoff, does not explicitly enter the NIBA expression, so the above short-time behavior persists to $t\to 0$. Except at $\alpha=\frac{1}{2}$, a spurious incoherent contribution in Eq. (23) dominates at

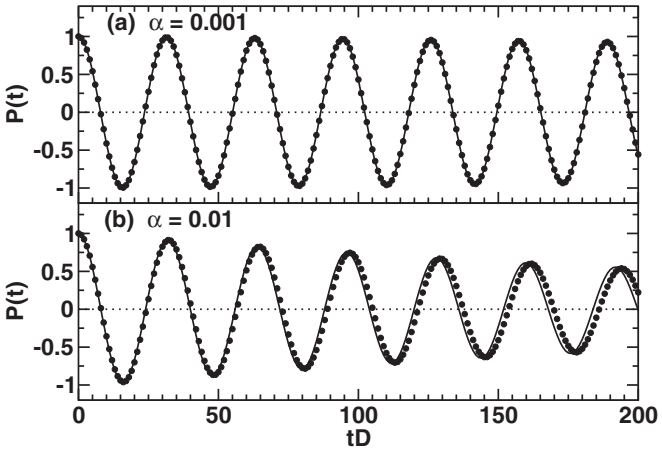

FIG. 8. $P(t)$ vs t in units of $1/D$ for (a) $\alpha = 0.001$ and (b) $\alpha = 0.01$. TDNRG (filled circles), NIBA (solid lines). The TDNRG results are obtained via the IRLM with a constant density of states $\rho = 1/2D$, $D = 1$, and $V/D = \Delta_0/\omega_c = 0.1$. NRG parameters: $\Lambda = 1.6$, $N_{\rm kept} = 2000$, and $n_z = 32$. The NIBA results were obtained from Eq. (23).

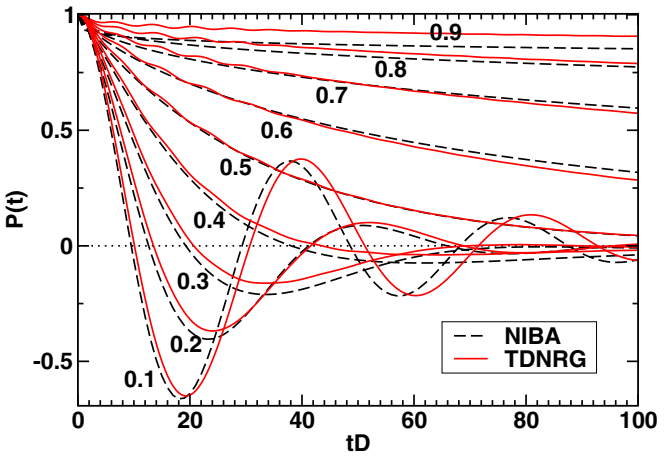

FIG. 9. Comparison between TDNRG (solid lines) and NIBA (dashed lines) results for $P(t)$ for $0.1 \leqslant \alpha \leqslant 0.9$. A constant density of states was used for the IRLM with $V/D = \Delta_0/\omega_c = 0.1$. NRG parameters as in Fig. 8.

asymptotically long times $t \gg 1/\Delta_{\rm eff}(\alpha)$, yielding a leading contribution behaving as $P(t) \sim -1/[\Delta_{\rm eff}(\alpha)t]^{2-2\alpha}$, whereas the correct behavior is an overall exponential decay of $P(t)$ for all α (with oscillatory terms contributing at $\alpha < \frac{1}{2}$) [28,42,43,92,93]. We shall elaborate in more detail on this in Sec. IV B 3 where we explain why the long-time errors in the TDNRG, studied extensively in Refs. [26,27], prohibit an accurate numerical investigation of the crossover from coherent to incoherent dynamics upon increasing α.

We come now to the comparisons. Figure 8 shows comparisons of TDNRG results for $P(t)$ (circles) at very weak dissipation strengths ($\alpha = 0.001$ and 0.01) with the corresponding NIBA predictions (lines). For $\alpha = 0.001$, both the frequency and decay rate of the oscillations match the NIBA result up to the longest times simulated (approximately 8 periods). The period of the oscillations is $T = 2\pi/\Omega_r(\alpha) \approx 2\pi/\Delta_0 = 10\pi$. The damping of the oscillations in the TDNRG is only marginally larger than those in the NIBA and is not visible on the scale of the plot for this particular case. For the somewhat stronger, but still very weak, dissipation strength of $\alpha = 0.01$, the NIBA data match those of the TDNRG in the first two periods, but thereafter the NIBA oscillations are in advance of the TDNRG ones, a point that we shall return to below.

With increasing $\alpha \gtrsim 0.1$, the agreement between TDNRG and NIBA first decreases for α values up to approximately 0.4, with the main differences being the stronger damping of the oscillations in the TDNRG (particularly for $\alpha = 0.2$, 0.3, and 0.4) and a tendency of the NIBA oscillations to advance over the TDNRG ones (particularly noticeable for $\alpha = 0.1$). Agreement then improves close to $\alpha = \frac{1}{2}$, and finally decreases again for larger α (see Fig. 9). The decreasing agreement for $\alpha > 0.6$ is consistent with expectations about the validity of the NIBA in this regime, which is not expected to be quantitatively accurate here. The decreasing agreement for increasing α up to 0.4 is more unexpected. The excellent agreement of TDNRG with TD-DMRG results in this region (see Fig. 12 in the following section) strongly suggests that the above differences are, in fact, due to the NIBA becoming inaccurate here. In order to further justify this statement, we proceed below to exclude several other possibilities.

First, we have checked that the TDNRG results are indeed converged with respect to the number of retained states $N_{\rm kept}$ and with respect to the discretization parameter Λ, used, where smaller Λ is known to give results closer to the continuum limit [25,26]. The results, shown in Figs. 21 and 22 of Appendix B, indicate converged results for the values used, $N_{\rm kept} = 2000$ and $\Lambda = 1.6$. Next, we checked that the TDNRG results for $P(t)$ are largely independent of the value of $\Delta_0/\omega_c = V/D$ used (see Fig. 20 of Appendix B). This indicates that the TDNRG results, like the NIBA, are in the scaling limit for all interesting time scales relative to $1/\Delta_{\rm eff}(\alpha)$. Differences between TDNRG and NIBA at ultrashort time scales $t \ll 1/D \ll 1/\Delta_{\rm eff}(\alpha)$ associated with the finite high-energy cutoff used in TDNRG calculations will be discussed in Sec. IV B 3. Such cutoff-dependent differences, while affecting the ultrashort time dynamics, cannot explain the deviations observed on time scales comparable to $1/\Delta_{\rm eff}(\alpha)$ between TDNRG and NIBA at $\alpha \sim 0.1$–0.4 [see Table II for a listing of $1/\Delta_{\rm eff}(\alpha)$].

Finally, neglecting for the moment the excellent agreement between the TDNRG and TD-DMRG results in the following section, we consider the possibility that the TDNRG oscillations could be in delay over the NIBA ones due to the finite error in the long-time limit of the former. This error increases monotonically with increasing α and is listed in Table II . The value of $P(\infty)$ should be exactly zero for an unbiased system, however, as discussed in detail elsewhere (see Refs. [26,27]), the long-time limit of TDNRG observables have a finite error.[6] In particular, some memory of our initial-state preparation

[6]This error arises from (a) the use of the NRG approximation and (b) from the use of a logarithmically discretized bath. The latter has a nonextensive heat capacity and cannot act as a proper heat bath for $\Lambda > 1$. It has been argued that this prevents relaxation of the system to the exact ground state of the final-state Hamiltonian [107].

TABLE II. Numerical value of the time scale $1/\Delta_{\rm eff}(\alpha)$ for different α. Also shown is the scale $1/T_0(\alpha)$, the ratio $\Delta_{\rm eff}(\alpha)/T_0(\alpha)$, and TDNRG results for $P(t\to\infty)=P(\infty)$ which gives the absolute error in the infinite-time limit of $P(t)$. All results are for a constant density of states as in Sec. IV B 1 and the NRG parameters are as in Fig. 8.

α	$1/\Delta_{\rm eff}(\alpha)$	$1/T_0(\alpha)$	$\Delta_{\rm eff}(\alpha)/T_0(\alpha)$	$P(\infty)$
0.001	5.008	5.018	1.002	0.000003
0.01	5.089	5.18	1.018	0.00016
0.1	6.11	6.97	1.141	0.0045
0.2	7.915	9.79	1.237	0.0092
0.3	11.098	14.38	1.296	0.0143
0.4	17.34	22.82	1.316	0.0186
0.5	31.83	40.92	1.286	0.0414
0.6	75.9	89.2	1.175	0.0407
0.7	288.6	270.4	0.940	0.049
0.8	3232	1541.9	0.477	0.0556
0.9	1032584	38800.0	0.038	0.066

$\sigma_z=+1$ is retained at long times, leading to a small positive value for $P(t\to\infty)$. Consequently, the oscillations at long times will not be exactly about the zero axis (dotted lines in Figs. 8 and 9), but somewhat shifted above this. In principle, this could lead to a delay of the TDNRG oscillations over the NIBA ones, but not on the time scales shown in Fig. 9, only at longer times when $P(t)\sim P(\infty)$. Moreover, a similar effect would have to be operative in the TD-DMRG results in order to explain why the agreement between TDNRG and TD-DMRG is so good, and yet they both disagree with the NIBA results. Since such an effect is not known in the TD-DMRG, we conclude that the reason for the discrepancy between NIBA and TDNRG for $0<\alpha<\frac{1}{2}$ is due to the simplicity of the former approximation. The discrepancy is not insignificant, e.g., for $\alpha=0.3$, there are large regions in the time domain on time scales $t\sim 1/\Delta_{\rm eff}(\alpha=0.3)$ where the relative error is 20%–30%. One can adjust $\Delta_{\rm eff}(\alpha)$ to fit NIBA and TDNRG results, however, this only approximately matches the frequencies and not the damping rates. The reason for this is that the functional form of $P_{\rm NIBA}(t)$, which depends only on α, differs from the correct one.

In Fig. 9, TDNRG results have been shown only up to $tD=100$ in order to facilitate comparisons with TD-DMRG results of the following section.[7] This time range includes the intermediate time scale $1/\Delta_{\rm eff}(\alpha)$ for all $\alpha\leqslant 0.6$ (see Table II), but for $\alpha\gtrsim 0.7$ this time scale lies outside of this range. We therefore show in Fig. 16 of Appendix B 2 a results for $P(t)$ extending up to $t\sim 10/\Delta_{\rm eff}(\alpha)$ for all α, demonstrating that the TDNRG can access times of order $1/\Delta_{\rm eff}(\alpha)$ for all α, albeit with significant errors at long times (tabulated in Table II).

Notice also a ringing effect at short times $t\gtrsim 1/D$ in the TDNRG results in Fig. 9 (particularly evident at large α), which is absent in the NIBA results. To a smaller extent, this ringing is also present in the TD-DMRG results to be presented below. It reflects the response of the system to a sudden quench at $t=0$ when the only relevant time scale before the onset of final-state correlations is the ultrashort time scale $1/D$ set by the high-energy cutoff (a time scale explicitly eliminated in the NIBA). The frequency of these oscillations is therefore comparable to D. Figure 19 in Appendix B 2 c shows these oscillations and their decay in more detail for the exactly solvable case of $\alpha=\frac{1}{2}$. They also occur in other models [25,26] with a hard cutoff, but appear absent (or less pronounced) in models which use a soft cutoff [e.g., for $J(\omega)=2\pi\alpha\omega\exp(-\omega/\omega_c)$] (see Ref. [39] for an example).

[7]For times longer than $tD=100$, the TD-DMRG calculations would require larger systems and correspondingly more computing resources to obtain numerically exact results.

2. Comparison with TD-DMRG

The TD-DMRG calculations for the IRLM were carried out using a tight-binding representation of the conduction band with constant hoppings $D/2$ along the chain. This corresponds to using a semielliptic density of states $\rho(\omega)=\frac{2}{\pi D^2}(D^2-\omega^2)^{1/2}\theta(D-|\omega|)$. By using the same choice of density of states in the TDNRG we can make a quantitative comparison of results for $P(t)$ with corresponding TD-DMRG results. Before showing these comparisons, we first check that we recover the same low-energy scale $T_0(\alpha)=1/2\chi(0)$ with $\chi(0)=-\partial n_d/\partial\varepsilon_d|_{\varepsilon_d=0}$ in both NRG and DMRG. For this purpose, we used a Wilson chain corresponding to a semielliptic band in both NRG and DMRG calculations. The results, shown in Fig. 10, indicate very good agreement over the whole range $0\leqslant\alpha\leqslant 0.9$. In practice, the TD-DMRG calculations reported below use a tight-binding chain of finite length $L=200$. While the low-energy scale in equilibrium DMRG $T_0(\alpha,L)$ still shows prominent finite-size effects at $L=200$ (see Fig. 17 of Appendix B 2 b), nevertheless, this is sufficient to converge the TD-DMRG results for $P(t)$ with respect to L for the time scales shown in the comparisons

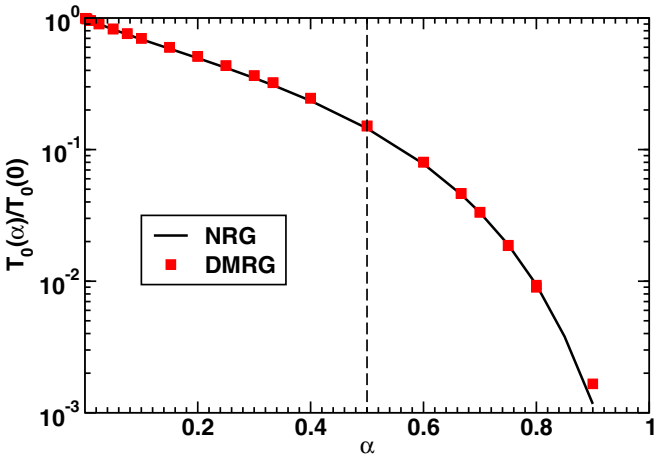

FIG. 10. The thermodynamic scale $T_0(\alpha)$ (normalized to its $\alpha=0$ value) vs α from NRG (solid line) and DMRG (squares). Both NRG and DMRG calculations were carried out for a semielliptic density of states $\rho(\omega)=\frac{2}{\pi D^2}\sqrt{D^2-\omega^2}$ using a Wilson chain representation of the conduction band. For NRG, $\Lambda=4$, $N_{\rm kept}=1062$, and $n_z=8$ were used, while for DMRG $\Lambda=1.6$ (without z averaging) was used. $T_0=1/2\chi(T=0)$ was calculated via a numerical derivative $\chi(T=0)=-\partial n_d/\partial\varepsilon_d|_{\varepsilon_d=0}\approx-\Delta n_d/\Delta\varepsilon_d$ with a sufficiently small increment $\Delta\varepsilon_d$ such that converged results were obtained.

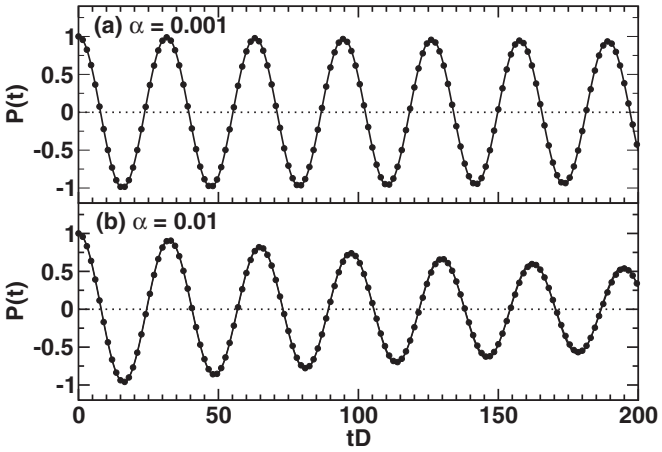

FIG. 11. Comparison between TDNRG (filled circles) and TD-DMRG (solid lines) for (a) $\alpha = 0.001$ and (b) $\alpha = 0.01$. NRG parameters as in Fig. 8. A semielliptic DOS is used and $V/D = \Delta_0/\omega_c = 0.1$. NRG parameters as in Fig. 8.

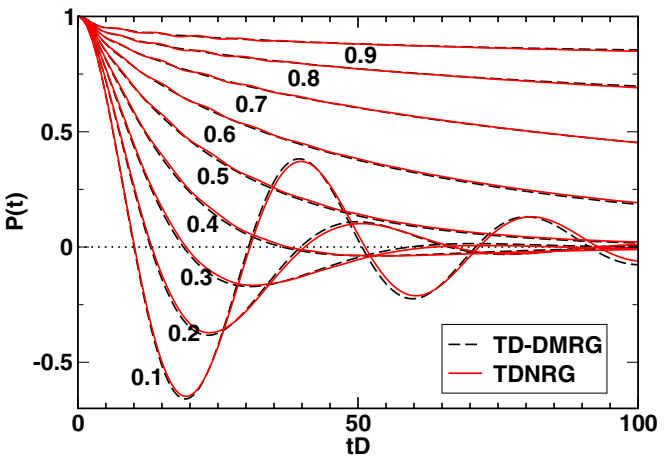

FIG. 12. Comparison of TDNRG (solid lines) and TD-DMRG (dashed lines) results for $P(t)$ for $\alpha = 0.1, \ldots, 0.9$. A semielliptic DOS is used and $V/D = \Delta_0/\omega_c = 0.1$. NRG parameters as in Fig. 8.

below ($tD \leqslant 100$). The reason for this is that the chosen initial state (see Sec. III) of reservoir plus impurity is influenced very little by the finite size of the reservoirs with respect to the boundary properties next to the impurity site (in contrast to the finite-size effects for the equilibrium unbiased $\varepsilon = 0$ system). For the time evolution, the Lieb-Robinson bounds ensure that information about the end of the chain can only travel through the reservoir at finite speed c (here the Fermi velocity) [94]. This defines a light cone of width ct around the impurity site outside of which the influence of the finiteness of the reservoirs is suppressed *exponentially*. Once this light cone reaches the end of the chain, prominent finite-size effects set in, but at all earlier times the results can be regarded to be in the thermodynamic limit for the local observables of interest here. To illustrate this, we refer the reader to Fig. 18 of Appendix B 2 b.

In Fig. 11, we compare TDNRG results for $P(t)$ (circles) at very weak dissipation ($\alpha = 0.001$ and 0.01) with corresponding TD-DMRG results (solid lines). The agreement is essentially perfect out to the longest times simulated, with both the frequency and damping rate of the oscillations being almost identical. For $\alpha = 0.01$, where we previously found that the NIBA oscillations advanced somewhat over the TDNRG ones, we here find perfect agreement between TD-DMRG and TDNRG.

With increasing α (see Fig. 12), the agreement between TDNRG and TD-DMRG continues to be very good at all times and up to the largest dissipation strength calculated ($\alpha = 0.9$). The TDNRG results for $0.1 \lesssim \alpha \lesssim 0.3$ exhibit a marginally larger damping than the TD-DMRG results. This could be due to the better description of the continuum, and hence the damping, within the latter approach on the time scales shown.[8] For $\alpha > 0.7$, and for the longest times $tD \sim 100$, one observes a tendency in Fig. 12 for the TD-DMRG results for $P(t)$ to lie marginally above the TDNRG ones. While the effect is marginal, it appears to be due to an upturn of the TD-DMRG results for longer times $tD \gtrsim 100$ (see Fig. 18 in Appendix B 2 b). For all intents and purposes, the results are converged with respect to L on the times scales of interest $tD \lesssim 100$. In contrast, the use of a Wilson chain in TDNRG simulates an essentially infinite (but discrete) system, and allows calculations to be carried out to arbitrarily long times, without significant finite-size effects, but with a finite error in this limit (see Table II and Fig. 16 in Appendix B 2 a). Notice also the ringing at short times $t \gtrsim 1/D$ with frequency of order D and discussed in the previous section. The oscillations correlate well for all α between TD-DMRG and TDNRG.

As noted previously, the NIBA expression $1 - P(t) \sim [\Delta_{\rm eff}(\alpha)t]^{2-2\alpha}$ for $t \ll 1/\Delta_{\rm eff}(\alpha)$, being in the scaling limit, is cutoff independent, since the cutoff ω_c has been absorbed into the low-energy scale $\Delta_{\rm eff}(\alpha)$. This means, in particular, that the short-time exponents $2 - 2\alpha$ persist in the whole range $0 \leqslant t \ll 1/\Delta_{\rm eff}(\alpha)$. In contrast, both TDNRG and TD-DMRG retain information about the finite high-energy cutoff D explicitly, thereby restricting the time range for observing the above exponents to $1/D \ll t \ll 1/\Delta_{\rm eff}(\alpha)$. Since the calculations in the present section used $V/D = \Delta_0/\omega_c = 0.1$, the energy window for extracting the above exponents is too small for most α.[9] In Sec. IV B 3, we shall use a much smaller V, thereby allowing the above exponents to be verified quantitatively.

[8] On the times $tD \leqslant 100$ of the comparisons, the tight-binding chain used in TD-DMRG with chain lengths $L = 200$ gives a better representation of the continuum conduction band than a Wilson chain with $\Lambda = 1.5$, which treats high energies with less resolution than the low energies (due to the use of a logarithmic mesh of energies about the Fermi level). Conversely, for sufficiently long times $tD > 100$, finite-size effects, discussed in Appendix B 2 b, are more pronounced in the TD-DMRG results.

[9] This choice of V was used in order to have comparable parameters as in the TD-DMRG calculations of Sec. IV B 2.

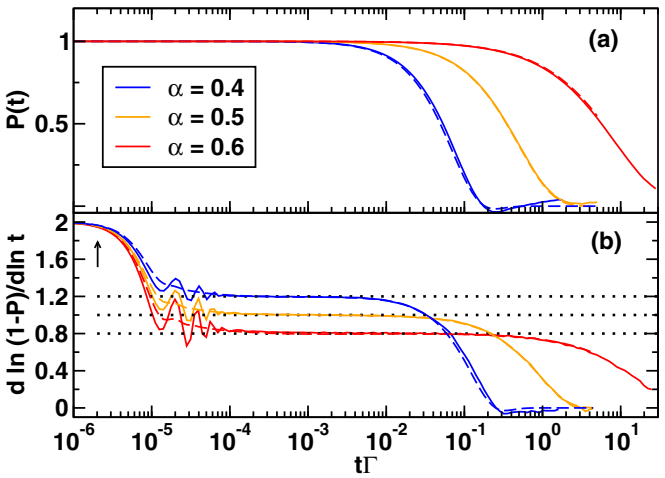

FIG. 13. (a) Comparison of TDNRG (solid lines) and FRG (dashed lines) results for $P(t)$ vs $t\Gamma$ in the region $\alpha \approx 0.5$, specifically for $\alpha = 0.4$, 0.5, and 0.6. We used a semielliptic density of states and $\Delta_0/\omega_c = V/D = 0.001$ corresponding (for $\alpha = \frac{1}{2}$) to a resonant level half-width of $\Gamma = 2\times10^{-6}$. In comparing results close to $\alpha = \frac{1}{2}$, measuring time in units of $1/\Gamma$ is useful since $\gamma_r(\frac{1}{2}) = \Delta_{\rm eff}(\frac{1}{2}) = 2\Gamma$. (b) Comparison of the logarithmic derivative $d\ln[1-P(t)]/d\ln t$ of $1-P(t)$ vs $t\Gamma$ from TDNRG (solid lines) and FRG (dashed lines) for the same α values as above. Black dotted lines indicate the short-time exponents $2(1-\alpha)$ in $1-P(t) \sim [\Delta_{\rm eff}(\alpha)t]^{2(1-\alpha)}$ for $1/D \ll t \ll 1/\Delta_{\rm eff}(\alpha)$. The vertical arrow indicates the ultrashort time scale $t = 1/D$ (in units of $1/\Gamma$). The logarithmic derivative magnifies the ringing effect, described in Secs. IV B 1 and IV B 2 and in Appendix B 2 c. NRG parameters as in Fig. 8.

3. Comparison with FRG

Close to $\alpha = \frac{1}{2}$ (corresponding to the vicinity of $U = 0$ in the IRLM), FRG calculations are well controlled and can be used to compare with TDNRG results for $P(t)$. Figure 13(a) shows these comparisons for $\alpha = 0.4$, 0.5, and 0.6 and $V/D = \Delta_0/\omega_c = 0.001$ where a semielliptic density of states has been used for both FRG and TDNRG.[10] For $\alpha = 0.5$, the agreement is particularly good at all times. FRG is exact in this limit, whereas TDNRG entails the usual approximation associated with neglecting high-energy states, hence, the small difference at $t \gtrsim 1/\Gamma$, where the bare resonant level half-width $\Gamma = \pi\rho(0)V^2$ is the relevant energy scale in this limit. Very good agreement is also found at $\alpha = 0.4$ and 0.6. Since these calculations were for $V/D = \Delta_0/\omega_c = 0.001$, it becomes possible to analyze the short-time limit $1/D \ll t \ll 1/\Delta_{\rm eff}(\alpha)$ in detail. In particular, it is now possible to extract the aforementioned exponents $2-2\alpha$ in the short-time behavior of $1-P(t) \sim [\Delta_{\rm eff}(\alpha)t]^{2-2\alpha}$ with t in the range $1/D \ll t \ll 1/\Delta_{\rm eff}(\alpha)$. That these exponents are recovered, both within FRG and TDNRG, can be seen in Fig. 13(b), which shows the logarithmic derivative $d\ln[1-P(t)]/d\ln(t)$.

Notice also that at ultrashort time scales $t \ll 1/D$, there are no bath degrees of freedom available to follow the dynamics of the two-level system. Therefore, the dynamics is of the form $P(t) \approx 1 - c_{\alpha_i}t^2$, similar to that of a noninteracting two-level system in the limit $t \to 0^+$ with an exponent 2 as found also numerically in Fig. 13(b). The prefactor c_{α_i} depends on the dissipative coupling α_i in the initial state, which for the present quench protocol (see Sec. III A) with $U_i = U_f$ is equal to the dissipative coupling in the final state $\alpha_f = \alpha$. For quantum quenches, where $\alpha_i \neq \alpha_f$, the ultrashort time behavior of $P(t)$ thus depends on α_i, whereas once system-bath correlations develop at $t \gtrsim 1/D$, a dependence of $P(t)$ on $\alpha_f = \alpha$ results.

Finally, we comment on why the TDNRG in its present formulation cannot be used to investigate the subtle issue of the crossover from coherent to incoherent dynamics [2,20]. It was recently shown [28,42] that this crossover is by far more complex than predicted by NIBA. In the latter, a single step transition from coherent dynamics with oscillatory behavior of $P(t)$ for all times to monotonic dynamics occurs at $\alpha = \frac{1}{2}$. However, using complementary RG methods, one of them being FRG, it was shown in Refs. [28,42,43] that the crossover from fully coherent to incoherent dynamics occurs via an intermediate regime with oscillatory behavior on short to intermediate times but monotonic behavior at large times (see also Ref. [92]). This regime was dubbed the partially coherent one. It would be very interesting to confirm this rich scenario using TDNRG. However, within both the NIBA, which predicts a crossover at $\alpha_c = \frac{1}{2}$, as well as the renormalization group approaches of Refs. [28,42], the quality factor of the oscillatory contributions to $P(t)$ is the same and is given by $Q = \Omega_r(\alpha)/\gamma_r(\alpha) = \cot\frac{\pi}{2}\frac{\alpha}{1-\alpha}$. In order to investigate this issue with the TDNRG, we require at the very least reliable results for $P(t)$ for two periods $t = 2T$ at $\alpha \approx 0.3$. At approximately this value of α, the transition from fully to partially coherent dynamics was found. Since $Q(0.3) \approx 1$ and $\Delta_{\rm eff}(0.3) \approx \gamma_r(0.3)$, we have that $P(2T) \approx P[4\pi/\Delta_{\rm eff}(0.3)] \approx P[13/\Delta_{\rm eff}(0.3)]$. On time scale $t = 13/\Delta_{\rm eff}(0.3) \gg 1/\Delta_{\rm eff}$, we can assume an exponential decay of $P(t)$ to obtain an upper bound estimate, i.e., using $P(t) \sim \exp[-\gamma_r(0.3)t] \approx \exp[-\Delta_{\rm eff}(0.3)t]$, we have that $P(2T) \approx \exp(-13) \approx 2\times10^{-6}$. Such an accuracy, is, however, not presently available within TDNRG, which for $\alpha = 0.3$ has a long-time error of $0.0143 \gg P(2T)$ (see Table II). This error starts to develop on a time scale of order $1/\gamma_r(\alpha)$, thereby making the investigation of the above issue impossible within the single-quench TDNRG formalism. In order to illustrate this, a comparison of TDNRG and FRG data for $|P(t)|$ in the partially coherent regime is shown on a log-log scale in Fig. 14. The dips correspond to zeros of $P(t)$, the vertical arrows indicate the NIBA time scale $1/\gamma_r(\alpha)$, and the horizontal dotted lines indicate the long-time error $P(\infty)$ in the TDNRG.[11] This comparison confirms the simple argument given above that the onset of errors at

[10] For a semielliptic density of states, the mapping of the IRLM to the Ohmic SBM is not rigorously valid, nevertheless, in the scaling limit $V/D \ll 1$, one expects the equivalence to hold on all time scales, except at $t \lesssim 1/D$. In extracting α from Table III, we use $\rho(0) = 1/\omega_c = 2/\pi$.

[11] Once $|P[t \gg 1/\gamma_r(\alpha)]| < |P(\infty)|$, TDNRG results are dominated by the finite long-time error and have no significance, hence, we show TDNRG data only up to $t \approx 7/\gamma_r(\alpha)$.

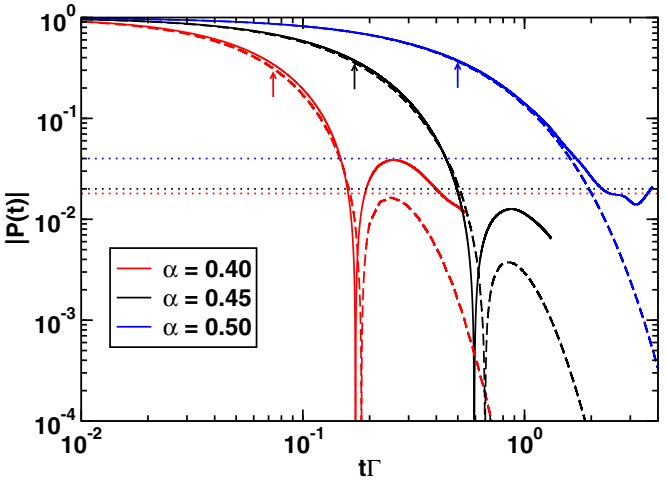

FIG. 14. Comparison of TDNRG (solid lines) and FRG (dashed lines) results for $|P(t)|$ vs $t\Gamma$ for $\alpha = 0.40$, 0.45, and 0.50 (in the partially coherent regime of Ref. [42]) on a log-log plot. Vertical arrows indicate the relaxation time scale $1/\gamma_r(\alpha)$ within the NIBA. Horizontal dotted lines indicate the long-time error $P(\infty)$ in the TDNRG results. TDNRG results are shown up to $t \approx 7/\gamma_r(\alpha)$, the typical time scale beyond which $|P(t)|$ has decayed to a value below the long-time error $|P(\infty)|$, and thus the data at longer times have no significance. We used a semielliptic density of states and $\Delta_0/\omega_c = V/D = 0.001$ corresponding (for $\alpha = \frac{1}{2}$) to a resonant level half-width of $\Gamma = 2\times10^{-6}$. NRG parameters as in Fig. 8.

$t \gtrsim 1/\gamma_r(\alpha)$ in TDNRG, studied in detail in Refs. [26,27] for the Anderson impurity model, prevents, in the present context, a detailed investigation of the crossover scenario from coherent to incoherent dynamics of Refs. [28,42,43]. On the other hand, the TDNRG results on time scales up to order $1/\gamma_r(\alpha)$ are also not inconsistent with such a picture.

V. CONCLUSIONS

In this paper, we investigated the thermodynamics and transient dynamics of the Ohmic two-state system, for dissipation strengths ranging from weak ($\alpha < \frac{1}{2}$) to strong ($\alpha > \frac{1}{2}$), by using the equivalence of this model to the IRLM. The IRLM, being a spinless fermionic model, is the simplest model that can capture the physics of the Ohmic two-state system in the interesting parameter regime $0 \leqslant \alpha < 1$. Within an NRG treatment of the IRLM, a larger fraction ($\frac{1}{2}$) of the states generated at each NRG iteration can be retained than is possible for other equivalent models, e.g., for the AKM (where approximately $\frac{1}{4}$ of the states can be retained). Consequently, more accurate and efficient calculations of the thermodynamics and transient dynamics of the Ohmic two-state system can be carried out by using the IRLM.

For the thermodynamics, we showed how the universal specific heat and susceptibility curves evolve with increasing dissipation strength α from the results for an isolated two-level system at vanishingly small dissipation $\alpha \to 0$, to the results for the isotropic Kondo model in the limit $\alpha \to 1^-$. The results recover in all cases the exact Fermi liquid behavior at $T \ll T_0(\alpha)$ and the known high-temperature asymptotics at $T \gg T_0(\alpha)$. Our results via the IRLM go beyond available Bethe ansatz calculations at rational values of α for the equivalent AKM [23] since they can be carried out for *arbitrary* dissipation strengths $0 \leqslant \alpha \leqslant 1^-$. Furthermore, we found very good agreement between NRG and DMRG calculations for the α dependence of T_0.

For the zero-temperature transient dynamics, we demonstrated excellent agreement on short to intermediate time scales for $P(t)$ between TDNRG and TD-DMRG for $0 \lesssim \alpha \lesssim 0.9$, and between TDNRG and FRG in the vicinity of $\alpha = \frac{1}{2}$. These comparisons (see Fig. 9) indicate that the TDNRG remains accurate, not only in limiting cases such as $t \to 0^+$, where it is known to be exact, but also at finite times $t \sim 1/\Delta_{\rm eff}(\alpha)$, and for general α where no exact results are available.

Finally, our comparisons between the NIBA and TDNRG allowed us to quantify the error in the former approximation for a range of α. While it is known that NIBA is not quantitatively correct in the incoherent regime $\alpha \gtrsim 0.5$, we found that there are significant errors of 20%–30% also in the range $0.1 \lesssim \alpha \lesssim 0.4$ for time scales comparable to $1/\Delta_{\rm eff}(\alpha)$. In contrast, the NIBA agrees well with TDNRG for $\alpha \approx \frac{1}{2}$ and for $\alpha \ll 1$ at short to intermediate times. In conclusion, our TDNRG results for $P(t)$ at general values of α and for short to intermediate time scales could serve as useful benchmarks for the development of new techniques to simulate the transient dynamics of spin-boson problems.

A major problem that still needs to be overcome within the TDNRG is that of obtaining accurate results for transient quantities at long times $t \gg 1/\gamma_r(\alpha)$, and in the asymptotically long-time limit $t \to \infty$ [25,26]. Progress on this, for example, within a multiple-quench generalization [27] or within hybrid TD-DMRG/TDNRG approaches [95], might allow issues such as the crossover from coherent to incoherent dynamics in the Ohmic two-state system to be investigated.

ACKNOWLEDGMENTS

We acknowledge financial support from the Deutsche Forschungsgemeinschaft via RTG 1995 and supercomputer support by the John von Neumann institute for Computing (Jülich) and the RWTH Computer Cluster. We would like to thank R. Bulla for discussions and sending us data from Ref. [45] which is used in Fig. 4.

APPENDIX A: EQUIVALENCE OF THE OHMIC SPIN-BOSON MODEL TO THE AKM, SPIN-FERMION MODEL, AND THE IRLM

For completeness, we here provide details of the equivalence of the Ohmic spin-boson model to a number of fermionic models via bosonization [21,96]. The basic bosonization identities that we use are summarized in Appendix A 1. For further details on bosonization, we refer the reader to the comprehensive overview of bosonization techniques in Ref. [97]. The procedure we follow is then to start with the AKM (Appendix A 2) and apply unitary transformations to map this model successively onto the SBM (Appendix A 3) and the IRLM (Appendix A 5). On the way, we also relate the SBM to the spin-fermion model (Appendix A 4).

1. Bosonization of free fermions

Consider first the free-fermion Hamiltonian

$$H_0 = \sum_{k\mu} \varepsilon_k c^\dagger_{k\mu} c_{k\mu}. \tag{A1}$$

We take a linear dispersion relation for the conduction electrons $\varepsilon_k = v_F k$ and measure k relative to the Fermi wave number k_F. We introduce fermion fields $\psi_\mu(x)$ via a Fourier series

$$\psi_\mu(x) = L^{-1/2} \sum_k e^{-ikx} c_{k\mu} \tag{A2}$$

with wave numbers $k = 2\pi n/L$, $n = 0, \pm 1, \ldots$, for periodic boundary conditions appropriate to a finite system of length L. The density of states per spin direction is given by $\rho = 1/2\pi v_F$. The kinetic energy can then be written as

$$H_0 = v_F \sum_{k,\mu} k\, c^\dagger_{k\mu} c_{k\mu} = i v_F \int_{-L/2}^{+L/2} \psi^\dagger_\mu(x) \partial_x \psi_\mu(x)\, dx. \tag{A3}$$

The fields $\psi_\mu(x)$ are expressed in terms of Hermitian bosonic fields $\varphi(x)$ in the standard way

$$\psi_\mu(x) = (2\pi a)^{-1/2} F_\mu e^{-i\varphi_\mu(x)}, \tag{A4}$$

where a is a cutoff, required for obtaining convergent momentum sums. The F_μ are the Klein factors required to ladder between states with different fermion number, and to ensure the correct anticommutation relations for the fermion fields [97,98], and

$$\varphi_\mu(x) = \phi_\mu(x) + \phi^\dagger_\mu(x), \tag{A5}$$

with the bosonic fields $\phi, \phi^\dagger$ given by

$$\phi^\dagger_\mu(x) = [\phi_\mu(x)]^\dagger \equiv -\sum_{q>0} n_q^{-1/2} e^{iqx} a^\dagger_{q\mu} e^{-aq/2}. \tag{A6}$$

Equation (A4) only holds as an operator identity if a is sent to zero, which thus has to be done at the end of every calculation. In the present context taking $a \to 0$ is equivalent to considering the scaling limit which explains why the mappings discussed below only hold in this limit. The a_q, $a^\dagger_q$, defined for $q > 0$, satisfy boson commutation relations with $n_q = (qL/2\pi)^{1/2}$, and are given by

$$a^\dagger_{q\mu} = (a_{q\mu})^\dagger = i\, n_q^{-1/2} \sum_k c^\dagger_{k+q\mu} c_{k\mu}. \tag{A7}$$

It is convenient to introduce spin and charge density operators in place of $a_{q\uparrow}$,$a_{q\downarrow}$ as follows:

$$a_{qC} = \frac{1}{\sqrt{2}}(a_{q\uparrow} + a_{q\downarrow}),$$

$$a_{qS} = \frac{1}{\sqrt{2}}(a_{q\uparrow} - a_{q\downarrow}).$$

The corresponding Hermitian fields are

$$\varphi_C = \frac{1}{\sqrt{2}}(\varphi_\uparrow + \varphi_\downarrow),$$

$$\varphi_S = \frac{1}{\sqrt{2}}(\varphi_\uparrow - \varphi_\downarrow),$$

with commutation relations

$$[\varphi_C(x), \varphi_S(x')] = 0, \tag{A8}$$

$$[\varphi_{C,S}(x), \partial_{x'}\varphi_{C,S}(x')] = 2\pi i \delta(x - x'). \tag{A9}$$

In terms of these, we have for the fields and densities

$$\psi_{C,S}(x) \equiv \frac{F_{C,S}}{\sqrt{2\pi a}} e^{-i\varphi_{C,S}(x)}, \tag{A10}$$

$$\rho_{C,S}(x) \equiv \psi^\dagger_{C,S}(x)\psi_{C,S}(x) = \frac{1}{2\pi}\partial_x \varphi_{C,S}(x). \tag{A11}$$

2. Bosonized anisotropic Kondo model

We start with the anisotropic Kondo model

$$H_{\mathrm{AKM}} = H_0 + H_\perp + H_\parallel \tag{A12}$$

with H_0 as above and

$$H_\perp = \frac{J_\perp}{2} \sum_{k,k'} (c^\dagger_{k\uparrow} c_{k'\downarrow}\, S^- + c^\dagger_{k\downarrow} c_{k'\uparrow}\, S^+),$$

$$H_\parallel = \frac{J_\parallel}{2} \sum_{k,k'} (c^\dagger_{k\uparrow} c_{k'\uparrow} - c^\dagger_{k\downarrow} c_{k'\downarrow}) S_z.$$

In terms of $\varphi_{C,S}$, we can write

$$\begin{aligned} H_0 &= v_F \sum_{q>0} q\, (a^\dagger_{q\uparrow} a_{q\uparrow} + a^\dagger_{q\downarrow} a_{q\downarrow}) \\ &= \frac{v_F}{2} \int_{-L/2}^{+L/2} \frac{dx}{2\pi} : [\partial_x \varphi_C(x)]^2 + [\partial_x \varphi_S(x)]^2 :, \\ H_\parallel &= \frac{J_\parallel}{2} S_z\, [\psi^\dagger_\uparrow(0)\psi_\uparrow(0) - \psi^\dagger_\downarrow(0)\psi_\downarrow(0)] \\ &= \frac{J_\parallel}{2} S_z \frac{1}{2\pi}\sqrt{2}\, \partial_x \varphi_S(0), \\ H_\perp &= \frac{J_\perp}{2} [\psi^\dagger_\uparrow(0)\psi_\downarrow(0)\, S^- + \psi^\dagger_\downarrow(0)\psi_\uparrow(0)\, S^+] \\ &= \frac{J_\perp}{4\pi a} (e^{i\sqrt{2}\varphi_s(0)} F_\uparrow F^\dagger_\downarrow\, S^- + e^{-i\sqrt{2}\varphi_s(0)} F_\downarrow F^\dagger_\uparrow\, S^+). \end{aligned}$$

We note that φ_C (which commutes with φ_S) does not couple to the impurity and only gives a contribution to the kinetic energy.

3. Equivalence to the Ohmic spin-boson model

We show that the unitary transformation $U = \exp[i\sqrt{2} S_z \varphi_S(0)]$ applied to H_{AKM} gives the spin-boson Hamiltonian H_{SBM} for Ohmic dissipation, i.e., that $U H_{\mathrm{AKM}} U^\dagger = H_{\mathrm{SBM}}$. We use the Baker-Hausdorff formula $e^{-B} A e^B = A + [A, B]$ with $[A, B]$ a c number and the commutation relations for φ_C,φ_S, to obtain

$$\begin{aligned} U H_0 U^\dagger &= H_0 - \sqrt{2} v_F S_z \frac{\partial \varphi_S}{\partial x}\bigg|_{x=0} = H_0 - \sqrt{2} v_F S_z \\ &\quad \times \sum_q \sqrt{\frac{2\pi q}{L}}\, (i a_{qS} + (i a_{qS})^\dagger)\, e^{-aq/2}, \\ U H_\parallel U^\dagger &= H_\parallel + \text{constant}, \end{aligned}$$

$$UH_\perp U^\dagger = \frac{J_\perp}{4\pi a}\,(e^{i\sqrt{2}\varphi_s(0)}F_\uparrow F_\downarrow^\dagger\, U S^- U^\dagger + e^{-i\sqrt{2}\varphi_s(0)}F_\downarrow F_\uparrow^\dagger\, U S^+ U^\dagger).$$

On using the identities

$$US^-U^\dagger = e^{-i\sqrt{2}\varphi_S(0)}S^-,$$
$$US^+U^\dagger = e^{i\sqrt{2}\varphi_S(0)}S^+,$$

and the representation $\frac{1}{2}\sigma^+ = F_\downarrow F_\uparrow^\dagger S^+$, $\sigma^- = (\sigma^+)^\dagger$, and $\frac{1}{2}\sigma_z = S_z$ of the Pauli spin operators, the term $UH_\perp U^\dagger$ becomes

$$UH_\perp U^\dagger = J_\perp \frac{1}{4\pi a}\,\sigma_x. \tag{A13}$$

We notice that a_{qC} does not couple to the impurity so we write $a_q = ia_{qS}$ and omit the charge density operators to obtain the Hamiltonian for the spin density excitations

$$H_{\rm SBM} = \frac{J_\perp}{4\pi a}\sigma_x + v_{\rm F}\sum_q q\, a_q^\dagger a_q + \left(\frac{J_\parallel}{4\pi} - v_{\rm F}\right)\sqrt{2}\frac{\sigma_z}{2}\sum_{q>0}\sqrt{\frac{2\pi q}{L}}\,(a_q + a_q^\dagger)\,e^{-aq/2}.$$

This is precisely the spin-boson model

$$H_{\rm SBM} = \sum_{q>0}\omega_q\, a_q^\dagger a_q - \frac{\Delta_0}{2}\sigma_x + \frac{q_0}{2}\sigma_z\sum_q \frac{C_q}{\sqrt{2m_q\omega_q}}(a_q + a_q^\dagger)$$

with $\omega_q = v_{\rm F}q$ and a spectral function for the harmonic oscillators

$$J(\omega) = \frac{\pi}{2}\sum_q \frac{C_q^2}{m_q\omega_q}\delta(\omega-\omega_q) = \frac{2\pi\alpha}{q_0^2}\,\omega\, e^{-\frac{\omega}{\omega_c}},$$

provided one chooses

$$\frac{C_q}{\sqrt{m_q}} = -\sqrt{\alpha}\frac{2}{q_0}\left(\frac{2\pi v_{\rm F}}{L}\right)^{1/2}\omega_q\, e^{-\frac{\omega_q}{2\omega_c}},$$

with a cutoff

$$\omega_c = \frac{v_{\rm F}}{a}.$$

One can identify the parameters

$$-\frac{\Delta_0}{2} = \frac{J_\perp}{4\pi a}$$

and

$$-\sqrt{\alpha} = \frac{J_\parallel}{4\pi v_{\rm F}} - 1,$$

which, together with the density of states (per spin) of the conduction electrons $\rho = 1/2\pi v_{\rm F}$ and the above definition of ω_c, result in the following identification of the dimensionless couplings of the two models

$$\frac{\Delta_0}{\omega_c} = -\rho J_\perp, \tag{A14}$$

$$\alpha = \left(1 - \frac{1}{2}\rho J_\parallel\right)^2. \tag{A15}$$

The sign of $J_\perp$ (or Δ_0) plays no role and we may choose $\Delta_0/\omega_c = +\rho J_\perp > 0$.

The precise form of Eq. (A15) depends on the specific regularization scheme used [21]. Within the framework of Abelian bosonization, the coupling $J_\parallel$ is directly proportional to the phase shifts $\rho J_\parallel = 4\delta/\pi$ [99]. For a finite-band model with cutoff $\omega_c = 2D$, the expression for the phase shift δ in terms of $\rho J_\parallel$ is given by $\delta = -\arctan(\pi\rho J_\parallel/4)$, and Eq. (A15) takes the form

$$\alpha = \left(1 + \frac{2}{\pi}\delta\right)^2. \tag{A16}$$

From the above equivalence, one sees that the AKM describes the physics of the Ohmic spin-boson model for dissipation strengths in the range $0 \leqslant \alpha \leqslant 4$ corresponding to $+\infty \leqslant J_\parallel \leqslant -\infty$ in the AKM.

4. Equivalence to the spin-fermion model

We note that, by replacing the bosonic bath in $H_{\rm SBM}$ above by a fermionic one, $H_0 = v_{\rm F}\sum_{q>0} q a_q^\dagger a_q \to \sum_{k\mu}\epsilon_k c_{k\mu}^\dagger c_{k\mu}$, and making use of the result for the spin density

$$S_{z,e}(0) = \frac{1}{2}\sum_{k,k'}(c_{k\uparrow}^\dagger c_{k'\uparrow} - c_{k\downarrow}^\dagger c_{k'\downarrow}) = \frac{1}{2}(c_\uparrow^\dagger c_\uparrow - c_\downarrow^\dagger c_\downarrow) = \frac{\sqrt{2}}{4\pi}\partial_x\varphi_S(0),$$

that we obtain a two-level system coupled to fermions (which we call the *spin-fermion* model)

$$H_{\rm SFM} = -\Delta_0 S_x + H_0 + J_z S_z S_z^e(0), \tag{A17}$$

with

$$\frac{1}{2}\rho J_z = 1 - \frac{1}{2}\rho J_\parallel = \sqrt{\alpha},$$
$$\frac{\Delta_0}{\omega_c} = \rho J_\perp,$$

or, expressed in terms of the phase shift $\delta = \arctan(\frac{\pi\rho J_z}{4})$ of conduction electrons scattering from the potential $J_z/4$:

$$\alpha = \left(\frac{2\delta}{\pi}\right)^2 = \left[\frac{2}{\pi}\arctan\left(\frac{\pi\rho J_z}{4}\right)\right]^2,$$

where $\rho = 1/2D$ is the conduction electron density of states per spin.[12] The spin-fermion model describes the physics of the Ohmic two-state system for dissipation strengths $0 \leqslant \alpha \leqslant 1$ corresponding to $0 \leqslant |J_z| \leqslant +\infty$. Finally, for a particle-hole symmetric conduction band $\epsilon_{-k} = -\epsilon_k$, making a particle-hole transformation on the down-spin electrons $c_k \to c_{-k}^\dagger$ allows the above model to be written so that the interaction term couples the two-level system coordinate S_z

[12] One can also start from the spin-fermion model (A17) and map this directly onto the AKM with the two successive unitary transformations $U_1 = \exp[i\sqrt{2}S_z\varphi_S(0)]$ and $U_2 = \exp(i\pi S_y)$ (A. Rosch, private communication) (see also Ref. [99]).

to the local electronic charge density $n_e(0) = c_\uparrow^\dagger c_\uparrow + c_\downarrow^\dagger c_\downarrow$ instead of the z component of the local electronic spin density. This form of the model is then suitable for describing the tunneling of atoms in metallic environments. Further generalizing this model to include electron-assisted tunneling terms [100] leads to non-Fermi-liquid two-channel Kondo behavior [101].

5. Equivalence to the IRLM

We start with the bosonized Kondo model $H_{\rm AKM}$ in terms of the fields $\varphi_{C,S}$ in Appendix A 2 and calculate $H_{\rm IRLM} = U H_{\rm AKM} U^\dagger$ with

$$U = \exp[i(\sqrt{2}-1)S_z\varphi(0)]. \tag{A18}$$

The calculation is similar to the previous one and we find

$$\begin{aligned} H_{\rm IRLM} = {} & v_{\rm F}\sum_{q>0} q a_{qS}^\dagger a_{qS} \\ & + \frac{J_\perp}{2\pi a}[e^{i\varphi(0)}\sigma^- + e^{-i\varphi(0)}\sigma^+] \\ & + \left(\frac{J_\parallel}{4\pi}\sqrt{2} - (\sqrt{2}-1)v_{\rm F}\right)\frac{\sigma^z}{2}\partial_x(0), \end{aligned}$$

with $\sigma^\pm$ as defined previously. In terms of the parameters of the spin-boson model, we have

$$\begin{aligned} H_{\rm IRLM} = {} & v_{\rm F}\sum_{q>0} q a_{qS}^\dagger a_{qS} + \pi v_{\rm F}(1-\sqrt{2\alpha})\sigma^z\rho_S(0) \\ & - \frac{\Delta_0}{2}[e^{i\varphi(0)}\sigma^- + e^{-i\varphi(0)}\sigma^+], \end{aligned}$$

where $\rho_S \equiv \rho_S(0) =: c_S^\dagger c_{S:} = \frac{1}{2}(c_S^\dagger c_S - c_S c_S^\dagger) + \text{const}$, is the density of a local spinless fermion field Ψ_S:

$$\Psi_S(0) \equiv c_S = \frac{1}{\sqrt{2\pi a}} F_S e^{i\varphi_S(0)}. \tag{A19}$$

We drop the index "S," replace the bosonic bath by a spinless free-fermion Hamiltonian $H_0^{\rm F} = v_{\rm F}\sum_k k c_k^\dagger c_k$, and identify $c = c_S = \frac{1}{\sqrt{L}}\sum_k c_k$ to obtain the interacting resonant level Hamiltonian

$$\begin{aligned} H_{\rm IRLM} = {} & v_{\rm F}\sum_k k c_k^\dagger c_k + V(d^\dagger c + c^\dagger d) \\ & + \frac{1}{2}\tilde{U}(d^\dagger d - d d^\dagger)(c^\dagger c - c c^\dagger). \end{aligned}$$

Here, we have replaced the spin operators $\sigma^\pm$ by fermion creation and annihilation operators $d = \frac{1}{2}F_S\sigma^+$, $d^\dagger = (d)^\dagger$ for a localized level at zero energy and we have made the identification $\sigma_z = d^\dagger d - d d^\dagger$. It can be seen that the parameters of the resonant level model are related to those of the Ohmic spin-boson model by

$$2\rho\tilde{U} = (1-\sqrt{2\alpha}), \tag{A20}$$

$$-\frac{\Delta_0}{2} = V, \tag{A21}$$

TABLE III. Parameter correspondence between the Ohmic SBM and the fermionic anistropic Kondo model (AKM), the spin-fermion model (SFM), and the interacting resonant level model (IRLM). The density of states $\rho = 1/2D$. For the spinfull fermionic models, h is a magnetic field which enters the respective Hamiltonians as a term of the form $-hS_z = -h\sigma_z/2$. The corresponding term in the IRLM is $\varepsilon_d n_d$.

SBM	AKM	SFM	IRLM
α	$(1+\frac{2\delta}{\pi})^2$, $\delta = \tan^{-1}(-\frac{\pi\rho J_\parallel}{4})$	$(\frac{2\delta}{\pi})^2$, $\delta = \tan^{-1}(\frac{\pi\rho J_z}{4})$	$\frac{1}{2}(1+\frac{2\delta}{\pi})^2$, $\delta = \tan^{-1}(-\frac{\pi\rho U}{2})$
Δ_0	$J_\perp$	Δ_0	$2V$
ω_c	$2D$	$2D$	$2D$
ϵ	h	h	ε_d

where as before $\rho = 1/2\pi v_{\rm F} = 1/\omega_c$. In terms of the bare resonant level width $\Gamma = \pi\rho V^2$, the last equation becomes

$$\pi\left(\frac{\Delta_0}{2\omega_c}\right)^2 = \frac{\Gamma}{\omega_c}. \tag{A22}$$

Replacing the potential $\rho\tilde{U}$ by the phase shift $\delta = -\arctan(\pi\rho\tilde{U})$ gives

$$\alpha = \frac{1}{2}\left(1+\frac{2\delta}{\pi}\right)^2, \tag{A23}$$

the relation used to connect the IRLM results in this paper to those for the Ohmic two-state system. Finally, note that in the paper we wrote the interaction term in the IRLM as $U(n_d - 1/2)(n_0 - 1/2)$, implying that $U = 2\tilde{U}$ so that $\delta = -\arctan(\pi\rho U/2)$ in Eq. (A23). One sees that the IRLM describes the physics of the Ohmic two-state system for dissipation strengths $0 \leqslant \alpha \leqslant 2$, corresponding to $+\infty \geqslant U \geqslant -\infty$ in the IRLM. Table III summarizes the parameter correspondence between the Ohmic spin-boson model and the three fermionic equivalents discussed in this Appendix.

APPENDIX B: ADDITIONAL RESULTS

We here provide some additional results for thermodynamics (Appendix B 1) and transient dynamics (Appendix B 2) in support of our conclusions in the main text.

1. Thermodynamics

Figure 15 illustrates the high-temperature asymptotics of the specific heat and static charge susceptibility of the IRLM at $T \gg T_0$ but still at $T \ll 2D$. The exponents $\nu_c = \nu_\chi = 2-2\alpha$ in Eqs. (19) and (21), extracted by numerical differentiation of the data, are generally well reproduced for all α (see Table I). At sufficiently high temperature $T \sim D$, not shown here, nonuniversal corrections arise due to the finite bandwidth used in the IRLM. These give rise, for example, at high enough temperatures to a negative impurity specific heat at finite $|U| > 0$, as found in many other models [102–105]. This does not contradict thermodynamic stability since the latter only requires that $C_{\rm tot}(T) \geqslant 0$ and $C_0(T) \geqslant 0$, which is guaranteed by construction, but the difference $C_{\rm imp}(T)$ can take any value.

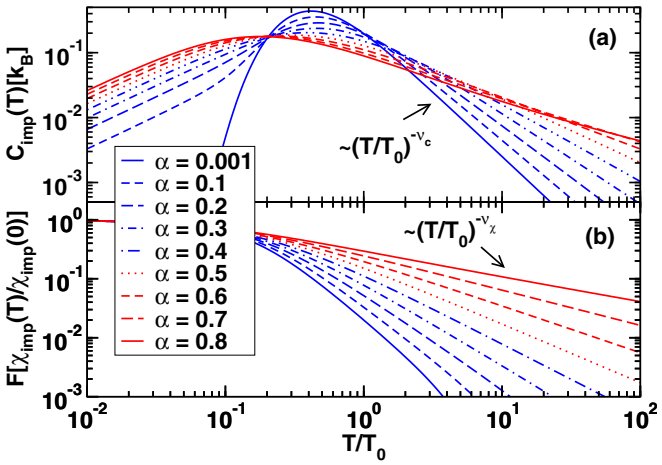

FIG. 15. Double-logarithmic plot for (a) specific heat $C_{\rm imp}(T)$ vs T/T_0, and (b) the quantity $F[\chi_{\rm imp}(T)/\chi_{\rm imp}(0)] \equiv 4\frac{T}{T_0}\frac{\chi_{\rm imp}(T)}{\chi_{\rm imp}(0)} - 1$ vs T/T_0 showing the high-temperature asymptotics $\sim(T/T_0)^{-\nu_{c,\chi}}$ of these quantities for $T/T_0 \gg 1$ with $\nu_c = \nu_\chi = 2 - 2\alpha$.

2. Transient dynamics

a. TDNRG results for $P(t)$ up to $t \sim 10/\Delta_{\rm eff}(\alpha)$

In Fig. 16, we show results for $P(t)$ extending up to times of order $t\,\Delta_{\rm eff}(\alpha) = 10$ for all α. This supports our statement in the main text that TDNRG can reach times of order $1/\Delta_{\rm eff}$ for all α. The scale $\Delta_{\rm eff}(\alpha)$, like the perturbative scale Δ_r, upon which it is based, is incorrect in the Kondo limit $\alpha \to 1^-$ (see Fig. 1, Table II, and Ref. [69]). In this limit, the dynamics is incoherent and we should expect that $\Delta_{\rm eff}(\alpha) \approx \gamma_r(\alpha)$, where $\gamma_r(\alpha)$ is the relaxation rate describing the decay of $P(t)$ at long times. Both scales, $\Delta_{\rm eff}(\alpha)$ and $\gamma_r(\alpha)$, should then be of order the thermodynamic Kondo scale $T_0(\alpha)$ in this limit (see Table II). However, for $\alpha \gtrsim 0.7$, it can be seen from Fig. 16 that $1/\Delta_{\rm eff}(\alpha)$ is not the relevant time scale for describing the decay of $P(t)$, being more than an order of magnitude too large for $\alpha = 0.9$. Instead, $1/T_0(\alpha)$, indicated by arrows in Fig. 16, sets the time scale for the decay of $P(t)$ for $\alpha \gtrsim 0.7$. We see that the TDNRG results appear accurate up to $t \sim 1/T_0(\alpha)$ for $\alpha \gtrsim 0.7$. Since such time scales are not accessible with the numerically exact TD-DMRG method for such large α, we cannot prove this. One sees, however, that the long-time limit errors of TDNRG become evident only at $t \gg 1/T_0(\alpha)$ for $\alpha = 0.9$. In general, we expect that the TDNRG will be accurate up to time scales of the order of the inverse decay rate (relaxation rate) $1/\gamma_r(\alpha)$ of the two-level system, which is the correct time scale for the approach to the long-time limit. For small $\alpha \ll 1$, this time scale can be much longer than $1/\Delta_{\rm eff}(\alpha)$, as seen from the NIBA expression for the relaxation rate $\gamma_r(\alpha) = \sin[\pi\alpha/2(1-\alpha)]\Delta_{\rm eff}(\alpha) \approx \pi\alpha\Delta_{\rm eff}(\alpha)/2 \ll \Delta_{\rm eff}(\alpha)$ for $\alpha \ll 1$. In this limit, TDNRG simulations remain accurate over many oscillations and can access times $t \gg 1/\Delta_{\rm eff}(\alpha)$ much longer than the "intermediate" time scale $1/\Delta_{\rm eff}(\alpha)$, but still shorter than the long time scale $1/\gamma_r(\alpha)$. Thus, the intermediate time scale $1/\Delta_{\rm eff}(\alpha)$ (suitably corrected for large $\alpha \gtrsim 0.7$) is a conservative estimate for the longest times up to which TDNRG results remain free of the errors associated with the approach to the long-time limit.

b. Dependence of TD-DMRG results on L

Figure 17 shows the convergence of the low-energy scale $T_0(\alpha, L)$ with increasing length L of the tight-binding chain used in the DMRG calculations. While the $L = 1000$ results show good convergence to the Wilson chain result, this length of chain would be numerically very expensive within a TD-DMRG calculation. However, due to the "Lieb-Robinson

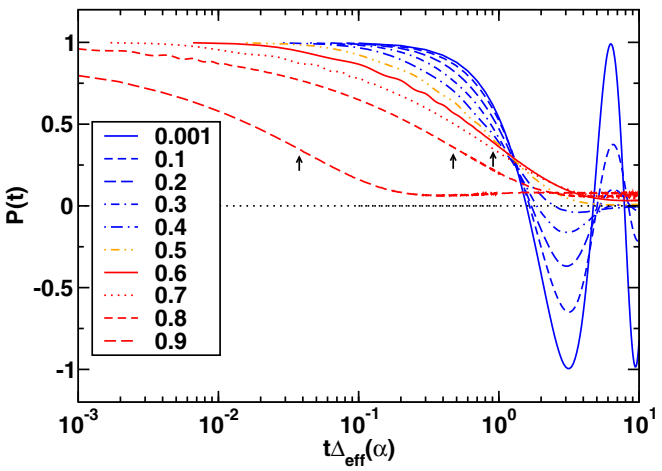

FIG. 16. $P(t)$ vs $t\,\Delta_{\rm eff}(\alpha)$ for the whole range of α (indicated in the legend). The results are the same as those in Sec. IV B 1 but with additional data extending the time range up to $10/\Delta_{\rm eff}(\alpha)$. The vertical arrows for the strong dissipation cases $\alpha = 0.7$, 0.8, and 0.9 indicate the time scale $1/T_0(\alpha)$ with $T_0(\alpha)$ taken from Fig. 1. The results are obtained via the IRLM with a constant density of states $\rho = 1/2D$, $D = 1$, and $V/D = \Delta_0/\omega_c = 0.1$. NRG parameters: $\Lambda = 1.6$, $N_{\rm kept} = 2000$, and $n_z = 32$.

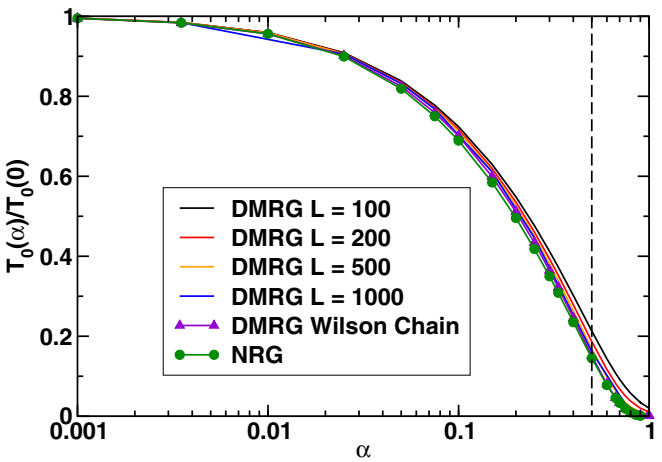

FIG. 17. Thermodynamic scale $T_0(\alpha, L)$ vs α for different tight-binding chain lengths ($L = 100$, 200, 500, 1000) in DMRG. Also shown are the DMRG and NRG results using a Wilson chain representation of a semielliptic DOS. The former used $\Lambda = 1.6$, while the latter used $\Lambda = 4$ and $n_z = 8$ (a smaller Λ was used in DMRG since z averaging is not used in the latter). In both approaches, $T_0 = 1/2\chi(T = 0)$ was calculated via a numerical derivative $\chi(T = 0) = -\partial n_d/\partial\varepsilon_d|_{\varepsilon_d=0} \approx -\Delta n_d/\Delta\varepsilon_d$ with a sufficiently small increment $\Delta\varepsilon_d$.

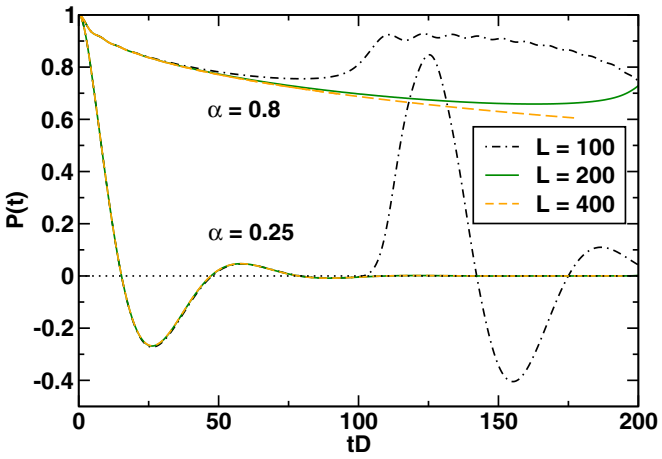

FIG. 18. Dependence of $P(t)$ on the size L of the tight-binding chain in TD-DMRG for $\alpha = 0.25$ and 0.8. For the time scales addressed in the main text $tD \leqslant 100$, a chain length of $L = 200$ suffices for $\alpha \lesssim 0.9$, while $L = 100$ would be too small.

bound" [94] one can employ shorter chains ($L = 200$) for the transient dynamics for the time scales shown as explained in the main text ($tD \lesssim 100$). This is illustrated in Fig. 18, which shows results for $P(t)$ at $\alpha = 0.25$ and 0.8. Converged results out to times $tD = 100$ are achieved for $L \geqslant 200$. In contrast, the chain of length $L = 100$ exhibits exhibits finite-size effects due to reflections from the end of the chain reaching the impurity on time scales $tD \sim 100$. Similar effects arise in other approaches, such as in studies of the transient dynamics of the Anderson model within an optimal basis approach, when the number of orbitals for the reservoir is not large enough [106]. By explicitly checking the L dependence of the TD-DMRG results, we confirmed that the results in the text for all α were converged for the times shown for $L = 200$.

c. *Ringing effect*

Figure 19 illustrates the ringing effect mentioned in the text for the exactly solvable case of $\alpha = \frac{1}{2}$. The analytic result for $P(t)$ can be evaluated for both a finite cutoff $\omega_c = 2D$ and in the so-called scaling limit $\omega_c \to \infty$, with the low-energy scale $\Delta_{\text{eff}}(\alpha = \frac{1}{2}) = 2\Gamma$ being kept constant [25]. The scaling limit result at $\alpha = \frac{1}{2}$, which is also the NIBA result, is simply $P(t) = \exp(-2\Gamma t)$. A finite high-energy cutoff $\omega_c = 2D$ introduces a new ultrashort time scale $1/D$ in the response of the system to a sudden switching and modifies the scaling limit result at short times. In Fig. 19, we show the corrections to the scaling limit result, i.e., $P(t) - \exp(-2\Gamma t)$. This measures the magnitude and decay of the ringing oscillations. As expected, their frequency is set by D. They decay as $1/t^3$ at long times $t \gg 1/D$. The TDNRG results exhibit similar oscillations, as do the TD-DMRG results. The latter are more damped, presumably because the use of a semielliptic DOS, corresponding to a tight-binding chain, is a more accurate description of the continuum bath than the Wilson chain of the TDNRG. Similary, the FRG data shown in Fig. 13 exhibit a much weaker ringing effect than the corresponding TDNRG data, again, presumably due to the use of a continuum bath in the FRG approach.

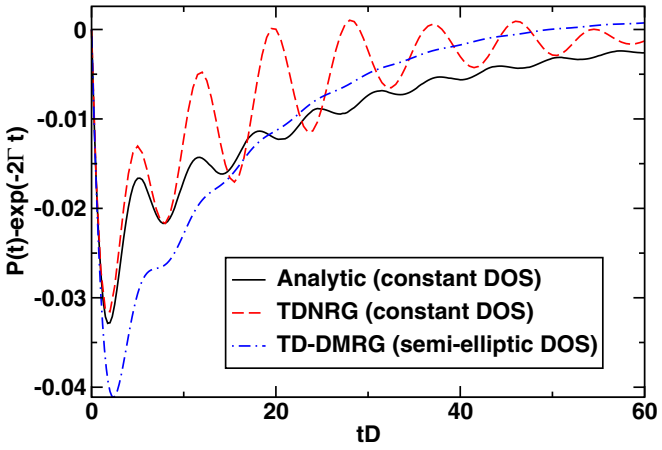

FIG. 19. $P(t) - \exp(-2\Gamma t)$ at $\alpha = \frac{1}{2}$ with $\Gamma = 0.02D$ and $P(t)$ calculated (i) analytically for a constant DOS $\rho(\omega) = 1/2D$, $-D \leqslant \omega \leqslant +D$ (black solid line), (ii) using TDNRG with a constant DOS (red dashed curve), and (iii) within TD-DMRG for a semielliptic DOS using a tight-binding chain of length $L = 200$ (blue dashed-dotted line).

d. *Dependence of TDNRG results on $\Delta_0/\omega_c = V/D$, N_{kept}, and Λ*

The NIBA is usually believed to provide a reasonable description of the short to intermediate time dynamics of $P(t)$ for $0 \lesssim \alpha \lesssim \frac{1}{2}$ [2,20]. In Sec. IV B 1, we found significant deviations between the NIBA and TDNRG results, particularly for $0.1 \lesssim \alpha \lesssim 0.4$. In order to exclude the possibility that this difference is due to nonconverged TDNRG results (with respect to the number of retained states N_{kept} or the value of Λ) or that the TDNRG results are not sufficiently deep in the scaling limit $\Delta_0/\omega_c \ll 1$, we performed various additional checks, as we now describe. In Fig. 20, we show the effect of decreasing $\Delta_0/\omega_c = 0.1$ by a factor of 10 on the TDNRG results for $P(t)$ at $\alpha = 0.1$, 0.2, and 0.3. We see that, on the

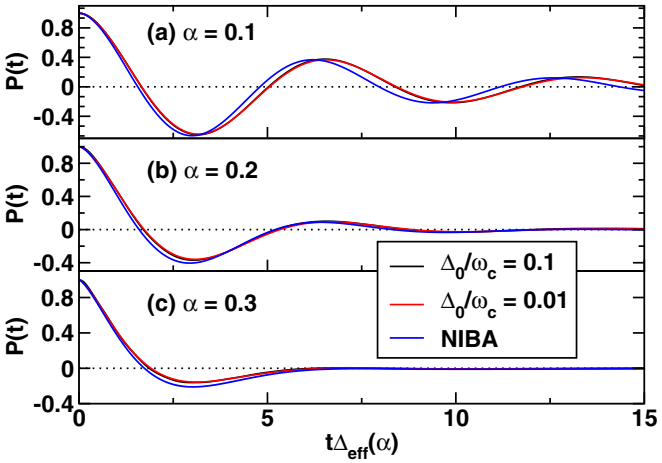

FIG. 20. Dependence of TDNRG results for $P(t)$ vs $t\Delta_{\text{eff}}(\alpha)$ on the ratio $V/D = \Delta_0/\omega_c$ for (a) $\alpha = 0.1$, (b) $\alpha = 0.2$, and (c) $\alpha = 0.3$. A constant density of states was used for the IRLM with $V/D = \Delta_0/\omega_c = 0.1$, and $V/D = \Delta_0/\omega_c = V/D = 0.01$. The NIBA results, which are independent of Δ_0/ω_c, are also shown. NRG parameters as in Fig. 8.

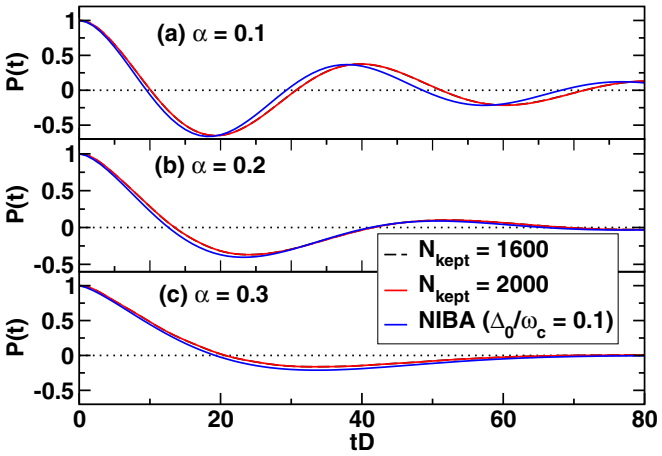

FIG. 21. Dependence of the TDNRG result for $P(t)$ on the number of kept states N_{kept} for (a) $\alpha = 0.1$, (b) $\alpha = 0.2$, and (c) $\alpha = 0.3$. A constant density of states was used for the IRLM with $V/D = \Delta_0/\omega_c = 0.1$. Also shown is the NIBA result. NRG parameters as in Fig. 8.

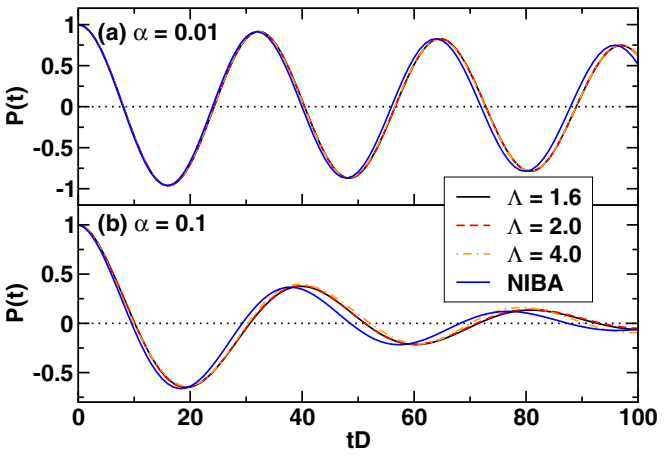

FIG. 22. Dependence of the TDNRG results for $P(t)$ vs t on the logarithmic discretization parameter Λ using $N_{\text{kept}} = 2000$ and $n_z = 32$, for (a) $\alpha = 0.01$ and (b) $\alpha = 0.1$. A constant density of states was used for the IRLM with $V/D = \Delta_0/\omega_c = 0.1$. Also shown is the NIBA result.

relevant time scales $t \sim 1/\Delta_{\text{eff}}(\alpha)$, the change in the TDNRG results is insignificant and much smaller than the observed differences with the NIBA results. This suggests that these differences are not due to the finite Δ_0/ω_c used in the TDNRG calculations, but represent quantitative differences between the TDNRG and NIBA results. We note that local quantities such as $n_d(t)$ in the IRLM [and hence $P(t) = 2n_d(t) - 1$] are less sensitive to band-edge effects than extensive quantities, such as specific heats $C_{\text{tot}}(T)$ and $C_0(T)$, and differences thereof such as $C_{\text{imp}}(T) = C_{\text{tot}}(T) - C_0(T)$. Thus, while in Sec. IV A universal results for $C_{\text{imp}}(T)$ required using $\Delta_0/\omega_c = V/D \ll 1$, for the local quantity $P(t)$, values of $\Delta_0/\omega_c = V/D = 0.1$ suffice to obtain universal results on the time scales of interest. Nonuniversal effects in $P(t)$, due to the finite cutoff D in the IRLM, only appear on time scales $t \lesssim 1/D$.

The dependence of the TDNRG results on the number of states is also seen to be insignificant for $N_{\text{kept}} \gtrsim 1600$ (see Fig. 21). A strong dependence of the TDNRG results on the number of retained states is only found if this number is taken to be too small, e.g., of the order 100 instead of the order 1000 as used in our calculations.

Finally, Fig. 22 shows the dependence of the TDNRG results on decreasing the logarithmic discretization parameter Λ for $\alpha = 0.01$ and 0.1. While the use of a smaller Λ better approximates the continuum bath at $\Lambda \to 1$, and hence can improve the long-time limit of TDNRG calculations [25–27], in practice one cannot take the limit $\Lambda \to 1$ since the loss in accuracy coming from the NRG truncation eventually outweighs any gains in approaching the continuum limit at $\Lambda \to 1$. The value $\Lambda = 1.6$, used here, therefore represents a compromise between these two effects. One sees from Fig. 22 that the results for $\Lambda = 2$ are almost indistinguishable to the $\Lambda = 1.6$ results, whereas those for $\Lambda = 4$, which correspond to a coarser description of the bath, start to show some deviation from the smaller Λ results. These deviations are particularly noticeable for the $\alpha = 0.1$ case. This motivated our use of $\Lambda = 1.6$ for all TDNRG calculations in this paper.

[1] A. O. Caldeira and A. J. Leggett, Quantum tunneling in a dissipative system, Ann. Phys. (NY) **149**, 374 (1983).
[2] A. J. Leggett, S. Chakravarty, A. T. Dorsey, M. P. A. Fisher, A. Garg, and W. Zwerger, Dynamics of the dissipative two-state system, Rev. Mod. Phys. **59**, 1 (1987).
[3] N. M. Zimmerman, B. Golding, and W. H. Haemmerle, Magnetic Field Tuned Energy of a Single Two-Level System in a Mesoscopic Metal, Phys. Rev. Lett. **67**, 1322 (1991).
[4] B. Golding, N. M. Zimmerman, and S. N. Coppersmith, Dissipative Quantum Tunneling of a Single Microscopic Defect in a Mesoscopic Metal, Phys. Rev. Lett. **68**, 998 (1992).
[5] J. Kondo, Diffusion of light interstitials in metals, Phys. B+C (Amsterdam) **125**, 279 (1984).
[6] H. Wipf and K. Neumaier, H and D Tunneling in Niobium, Phys. Rev. Lett. **52**, 1308 (1984).
[7] H. Grabert and H. R. Schober, Theory of tunneling and diffusion of light interstitials in metals, in *Hydrogen in Metals III*, edited by Helmut Wipf, Topics in Applied Physics (Springer, Berlin, 1997), Vol. 73, pp. 5–49.
[8] A. J. Leggett, in *Percolation, Localization and Superconductivity*, edited by M. Goldman and S. A. Wolf, NATO Advanced Study Institute, Series B: Physics (Plenum, New York, 1984), Vol. 109, pp. 1–42.
[9] A. LeClair, F. Lesage, S. Lukyanov, and H. Saleur, The Maxwell-Bloch theory in quantum optics and the Kondo model, Phys. Lett. A **235**, 203 (1997).
[10] K. L. Hur, Kondo resonance of a microwave photon, Phys. Rev. B **85**, 140506 (2012).
[11] M. Goldstein, M. H. Devoret, M. Houzet, and L. I. Glazman, Inelastic Microwave Photon Scattering Off a Quantum Impurity

in a Josephson-Junction Array, Phys. Rev. Lett. **110**, 017002 (2013).
[12] B. Peropadre, D. Zueco, D. Porras, and J. J. García-Ripoll, Nonequilibrium and Nonperturbative Dynamics of Ultrastrong Coupling in Open Lines, Phys. Rev. Lett. **111**, 243602 (2013).
[13] I. Snyman and S. Florens, Robust josephson-kondo screening cloud in circuit quantum electrodynamics, Phys. Rev. B **92**, 085131 (2015).
[14] S. Bera, H. U. Baranger, and S. Florens, Dynamics of a qubit in a high-impedance transmission line from a bath perspective, Phys. Rev. A **93**, 033847 (2016).
[15] N. Gheeraert, S. Bera, and S. Florens, Spontaneous emission of many-body Schrödinger cats in metamaterials with large fine structure constant, arXiv:1601.01545.
[16] H. Paik, D. I. Schuster, L. S. Bishop, G. Kirchmair, G. Catelani, A. P. Sears, B. R. Johnson, M. J. Reagor, L. Frunzio, L. I. Glazman, S. M. Girvin, M. H. Devoret, and R. J. Schoelkopf, Observation of High Coherence in Josephson Junction Qubits Measured in a Three-Dimensional Circuit Qed Architecture, Phys. Rev. Lett. **107**, 240501 (2011).
[17] D. Loss and D. P. DiVincenzo, Quantum computation with quantum dots, Phys. Rev. A **57**, 120 (1998).
[18] R. A. Marcus and N. Sutin, Electron transfers in chemistry and biology, Rev. Bioenerg. **811**, 265 (1985).
[19] S. Tornow, R. Bulla, F. B. Anders, and A. Nitzan, Dissipative two-electron transfer: A numerical renormalization group study, Phys. Rev. B **78**, 035434 (2008).
[20] U. Weiss, *Quantum Dissipative Systems* (World Scientific, Singapore, 2008), Vol. 13.
[21] F. Guinea, V. Hakim, and A. Muramatsu, Bosonization of a two-level system with dissipation, Phys. Rev. B **32**, 4410 (1985).
[22] P. B. Vigman and A. M. Finkelstein, Resonant-level model in the kondo problem, Zh. Eksp. Teor. Fiz. **75**, 204 (1978) [Sov. Phys.–JETP **48**, 102 (1978)].
[23] T. A. Costi and G. Zarand, Thermodynamics of the dissipative two-state system: A bethe-ansatz study, Phys. Rev. B **59**, 12398 (1999).
[24] F. B. Anders and A. Schiller, Real-Time Dynamics in Quantum-Impurity Systems: A Time-Dependent Numerical Renormalization-Group Approach, Phys. Rev. Lett. **95**, 196801 (2005).
[25] F. B. Anders and A. Schiller, Spin precession and real-time dynamics in the kondo model: Time-dependent numerical renormalization-group study, Phys. Rev. B **74**, 245113 (2006).
[26] H. T. M. Nghiem and T. A. Costi, Generalization of the time-dependent numerical renormalization group method to finite temperatures and general pulses, Phys. Rev. B **89**, 075118 (2014).
[27] H. T. M. Nghiem and T. A. Costi, Time-dependent numerical renormalization group method for multiple quenches: Application to general pulses and periodic driving, Phys. Rev. B **90**, 035129 (2014).
[28] D. M. Kennes, O. Kashuba, M. Pletyukhov, H. Schoeller, and V. Meden, Oscillatory Dynamics and Non-Markovian Memory in Dissipative Quantum Systems, Phys. Rev. Lett. **110**, 100405 (2013).
[29] R. Görlich and U. Weiss, Specific heat of the dissipative two-state system, Phys. Rev. B **38**, 5245 (1988).
[30] T. Kato and M. Imada, Quantum effects of resistance-shunted josephson junctions, J. Phys. Soc. Jpn. **69**, 203 (2000).
[31] T. A. Costi, Scaling and Universality in the Anisotropic Kondo Model and the Dissipative Two-State System, Phys. Rev. Lett. **80**, 1038 (1998).
[32] A. M. Tsvelick and P. B. Wiegmann, Exact results in the theory of magnetic alloys, Adv. Phys. **32**, 453 (1983).
[33] V. L. Campo and L. N. Oliveira, Alternative discretization in the numerical renormalization-group method, Phys. Rev. B **72**, 104432 (2005).
[34] L. Merker, A. Weichselbaum, and T. A. Costi, Full density-matrix numerical renormalization group calculation of impurity susceptibility and specific heat of the anderson impurity model, Phys. Rev. B **86**, 075153 (2012).
[35] R. Egger and C. H. Mak, Low-temperature dynamical simulation of spin-boson systems, Phys. Rev. B **50**, 15210 (1994).
[36] D. E. Makarov and N. Makri, Path integrals for dissipative systems by tensor multiplication. Condensed phase quantum dynamics for arbitrarily long time, Chem. Phys. Lett. **221**, 482 (1994).
[37] N. Makri and D. E. Makarov, Tensor propagator for iterative quantum time evolution of reduced density matrices. I. Theory, J. Chem. Phys. **102**, 4600 (1995).
[38] N. Makri, Numerical path integral techniques for long time dynamics of quantum dissipative systems, J. Math. Phys. **36**, 2430 (1995).
[39] H. Wang and M. Thoss, From coherent motion to localization: Dynamics of the spin-boson model at zero temperature, New J. Phys. **10**, 115005 (2008).
[40] S. Weiss, J. Eckel, M. Thorwart, and R. Egger, Iterative real-time path integral approach to nonequilibrium quantum transport, Phys. Rev. B **77**, 195316 (2008).
[41] P. P. Orth, A. Imambekov, and K. L. Hur, Nonperturbative stochastic method for driven spin-boson model, Phys. Rev. B **87**, 014305 (2013).
[42] D. M. Kennes, O. Kashuba, and V. Meden, Dynamical regimes of dissipative quantum systems, Phys. Rev. B **88**, 241110 (2013).
[43] O. Kashuba and H. Schoeller, Transient dynamics of open quantum systems, Phys. Rev. B **87**, 201402 (2013).
[44] R. Bulla, N.-H. Tong, and M. Vojta, Numerical Renormalization Group for Bosonic Systems and Application to the Sub-Ohmic Spin-Boson Model, Phys. Rev. Lett. **91**, 170601 (2003).
[45] R. Bulla, H.-J. Lee, N.-H. Tong, and M. Vojta, Numerical renormalization group for quantum impurities in a bosonic bath, Phys. Rev. B **71**, 045122 (2005).
[46] M. T. Glossop and K. Ingersent, Numerical Renormalization-Group Study of the Bose-Fermi Kondo Model, Phys. Rev. Lett. **95**, 067202 (2005).
[47] M. T. Glossop and K. Ingersent, Kondo physics and dissipation: A numerical renormalization-group approach to bose-fermi kondo models, Phys. Rev. B **75**, 104410 (2007).
[48] C.-H. Chung, M. T. Glossop, L. Fritz, M. Kirćan, K. Ingersent, and M. Vojta, Quantum phase transitions in a resonant-level model with dissipation: Renormalization-group studies, Phys. Rev. B **76**, 235103 (2007).
[49] P. P. Orth, D. Roosen, W. Hofstetter, and K. L. Hur, Dynamics, synchronization, and quantum phase transitions of two dissipative spins, Phys. Rev. B **82**, 144423 (2010).

[50] K. L. Hur, Entanglement entropy, decoherence, and quantum phase transitions of a dissipative two-level system, Ann. Phys. (NY) **323**, 2208 (2008).

[51] L. N. Oliveira and J. W. Wilkins, Specific Heat of the Kondo Model, Phys. Rev. Lett. **47**, 1553 (1981).

[52] L. Borda, A. Schiller, and A. Zawadowski, Applicability of bosonization and the anderson-yuval methods at the strong-coupling limit of quantum impurity problems, Phys. Rev. B **78**, 201301 (2008).

[53] A. Kiss, J. Otsuki, and Y. Kuramoto, Scaling theory vs exact numerical results for spinless resonant level model, J. Phys. Soc. Jpn. **82**, 124713 (2013).

[54] L. Borda, K. Vladár, and A. Zawadowski, Theory of a resonant level coupled to several conduction-electron channels in equilibrium and out of equilibrium, Phys. Rev. B **75**, 125107 (2007).

[55] B. Doyon, New Method for Studying Steady States in Quantum Impurity Problems: The Interacting Resonant Level Model, Phys. Rev. Lett. **99**, 076806 (2007).

[56] E. Boulat and H. Saleur, Exact low-temperature results for transport properties of the interacting resonant level model, Phys. Rev. B **77**, 033409 (2008).

[57] E. Boulat, H. Saleur, and P. Schmitteckert, Twofold Advance in the Theoretical Understanding of Far-From-Equilibrium Properties of Interacting Nanostructures, Phys. Rev. Lett. **101**, 140601 (2008).

[58] A. Nishino, T. Imamura, and N. Hatano, Exact Scattering Eigenstates, Many-Body Bound States, and Nonequilibrium Current in an Open Quantum Dot System, Phys. Rev. Lett. **102**, 146803 (2009).

[59] C. Karrasch, M. Pletyukhov, L. Borda, and V. Meden, Functional renormalization group study of the interacting resonant level model in and out of equilibrium, Phys. Rev. B **81**, 125122 (2010).

[60] S. Andergassen, M. Pletyukhov, D. Schuricht, H. Schoeller, and L. Borda, Renormalization group analysis of the interacting resonant-level model at finite bias: Generic analytic study of static properties and quench dynamics, Phys. Rev. B **83**, 205103 (2011).

[61] C. Karrasch, S. Andergassen, M. Pletyukhov, D. Schuricht, L. Borda, V. Meden, and H. Schoeller, Non-equilibrium current and relaxation dynamics of a charge-fluctuating quantum dot, Europhys. Lett. **90**, 30003 (2010).

[62] D. M. Kennes, S. G. Jakobs, C. Karrasch, and V. Meden, Renormalization group approach to time-dependent transport through correlated quantum dots, Phys. Rev. B **85**, 085113 (2012).

[63] D. M. Kennes and V. Meden, Interacting resonant-level model in nonequilibrium: Finite-temperature effects, Phys. Rev. B **87**, 075130 (2013).

[64] S. T. Carr, P. Schmitteckert, and H. Saleur, Full counting statistics in the not-so-long-time limit, Phys. Scr. **2015**, 014009 (2015).

[65] A. Nishino, N. Hatano, and G. Ordonez, Universal electric current of interacting resonant-level models with asymmetric interactions: An extension of the landauer formula, Phys. Rev. B **91**, 045140 (2015).

[66] A. Kiss, Y. Kuramoto, and J. Otsuki, Exact dynamics of charge fluctuations in the multichannel interacting resonant level model, J. Phys. Soc. Jpn. **84**, 104602 (2015).

[67] A. J. Bray and M. A. Moore, Influence of Dissipation on Quantum Coherence, Phys. Rev. Lett. **49**, 1545 (1982).

[68] P. W. Anderson, G. Yuval, and D. R. Hamann, Exact results in the kondo problem. ii. scaling theory, qualitatively correct solution, and some new results on one-dimensional classical statistical models, Phys. Rev. B **1**, 4464 (1970).

[69] T. A. Costi and C. Kieffer, Equilibrium Dynamics of the Dissipative Two-State System, Phys. Rev. Lett. **76**, 1683 (1996).

[70] K. G. Wilson, The renormalization group: Critical phenomena and the kondo problem, Rev. Mod. Phys. **47**, 773 (1975).

[71] H. R. Krishna-Murthy, J. W. Wilkins, and K. G. Wilson, Renormalization-group approach to the anderson model of dilute magnetic alloys. I. Static properties for the symmetric case, Phys. Rev. B **21**, 1003 (1980).

[72] R. Bulla, T. A. Costi, and T. Pruschke, Numerical renormalization group method for quantum impurity systems, Rev. Mod. Phys. **80**, 395 (2008).

[73] W. C. Oliveira and L. N. Oliveira, Generalized numerical renormalization-group method to calculate the thermodynamical properties of impurities in metals, Phys. Rev. B **49**, 11986 (1994).

[74] C. Gonzalez-Buxton and K. Ingersent, Renormalization-group study of anderson and kondo impurities in gapless fermi systems, Phys. Rev. B **57**, 14254 (1998).

[75] T. A. Costi, Renormalization-group approach to nonequilibrium green functions in correlated impurity systems, Phys. Rev. B **55**, 3003 (1997).

[76] A. Weichselbaum and J. von Delft, Sum-Rule Conserving Spectral Functions from the Numerical Renormalization Group, Phys. Rev. Lett. **99**, 076402 (2007).

[77] A. Weichselbaum, Tensor networks and the numerical renormalization group, Phys. Rev. B **86**, 245124 (2012).

[78] U. Schollwöck, The density-matrix renormalization group, Rev. Mod. Phys. **77**, 259 (2005).

[79] U. Schollwöck, The density-matrix renormalization group in the age of matrix product states, Ann. Phys. (NY) **326**, 96 (2011).

[80] J. R. Taylor, *Scattering Theory* (Wiley, New York, 1972).

[81] H.-U. Desgranges and K. D. Schotte, Specific heat of the kondo model, Phys. Lett. A **91**, 240 (1982).

[82] D. Vollhardt, Characteristic Crossing Points in Specific Heat Curves of Correlated Systems, Phys. Rev. Lett. **78**, 1307 (1997).

[83] R. Görlich and U. Weiss, Thermodynamics of the two-state system coupled weakly to conduction electrons, Il Nuovo Cimento D **11**, 123 (1989).

[84] H-U. Desgranges, Thermodynamics of the n-channel kondo problem (numerical solution), J. Phys. C: Solid State Phys. **18**, 5481 (1985).

[85] A. M. Tsvelick and P. B. Wiegmann, Low-temperature properties of the asymmetric anderson model (exact solution) ii, Phys. Lett. A **89**, 368 (1982).

[86] A. C. Hewson, *The Kondo Problem to Heavy Fermions* (Cambridge University Press, Cambridge, 1997).

[87] M. A. Cazalilla and J. B. Marston, Time-Dependent Density-Matrix Renormalization Group: A Systematic Method for the Study of Quantum Many-Body Out-of-Equilibrium Systems, Phys. Rev. Lett. **88**, 256403 (2002).

[88] H. G. Luo, T. Xiang, and X. Q. Wang, Comment on Time-Dependent Density-Matrix Renormalization Group: A Systematic Method for the Study of Quantum Many-Body Out-of-Equilibrium Systems, Phys. Rev. Lett. **91**, 049701 (2003).

[89] A J Daley, C Kollath, U Schollwöck, and G Vidal, Time-dependent density-matrix renormalization-group using adaptive effective hilbert spaces, J. Stat. Mech. (2004) P04005.

[90] S. R. White and A. E. Feiguin, Real-Time Evolution Using the Density Matrix Renormalization Group, Phys. Rev. Lett. **93**, 076401 (2004).

[91] W. Metzner, M. Salmhofer, C. Honerkamp, V. Meden, and K. Schönhammer, Functional renormalization group approach to correlated fermion systems, Rev. Mod. Phys. **84**, 299 (2012).

[92] R. Egger, H. Grabert, and U. Weiss, Crossover from coherent to incoherent dynamics in damped quantum systems, Phys. Rev. E **55**, R3809 (1997).

[93] F. Lesage and H. Saleur, Boundary Interaction Changing Operators and Dynamical Correlations in Quantum Impurity Problems, Phys. Rev. Lett. **80**, 4370 (1998).

[94] E. H. Lieb and D. W. Robinson, The finite group velocity of quantum spin systems, Commun. Math. Phys. **28**, 251 (1972).

[95] F. Güttge, F. B. Anders, U. Schollwöck, E. Eidelstein, and A. Schiller, Hybrid nrg-dmrg approach to real-time dynamics of quantum impurity systems, Phys. Rev. B **87**, 115115 (2013).

[96] P. Schlottmann, The kondo problem. I. Transformation of the model and its renormalization, Phys. Rev. B **25**, 4815 (1982).

[97] J von Delft and H Schoeller, Bosonization for beginners - refermionization for experts, Ann. Phys. (Berlin) **7**, 225 (1998).

[98] G. Kotliar and Q. Si, Toulouse points and non-Fermi-liquid states in the mixed-valence regime of the generalized Anderson model, Phys. Rev. B **53**, 12373 (1996).

[99] V. J. Emery and S. Kivelson, Mapping of the two-channel kondo problem to a resonant-level model, Phys. Rev. B **46**, 10812 (1992).

[100] K. Vladár and A. Zawadowski, Theory of the interaction between electrons and the two-level system in amorphous metals. I. Noncommutative model hamiltonian and scaling of first order, Phys. Rev. B **28**, 1564 (1983).

[101] G. Zaránd, T. Costi, A. Jerez, and N. Andrei, Thermodynamics of the anisotropic two-channel kondo problem, Phys. Rev. B **65**, 134416 (2002).

[102] S. Florens and A. Rosch, Climbing the Entropy Barrier: Driving the Single- Towards the Multichannel Kondo Effect by a Weak Coulomb Blockade of the Leads, Phys. Rev. Lett. **92**, 216601 (2004).

[103] R. Zitko and T. Pruschke, Anomaly in the heat capacity of kondo superconductors, Phys. Rev. B **79**, 012507 (2009).

[104] G.-L. Ingold, P. Hänggi, and P. Talkner, Specific heat anomalies of open quantum systems, Phys. Rev. E **79**, 061105 (2009).

[105] G. Ingold, Thermodynamic anomaly of the free damped quantum particle: The bath perspective, Eur. Phys. J. B **85**, 1 (2012).

[106] C. Lin and A. A. Demkov, Quench dynamics of anderson impurity model using configuration interaction method, Phys. Rev. B **92**, 155135 (2015).

[107] A. Rosch, Wilson chains are not thermal reservoirs, Eur. Phys. J. B **85**, 1 (2012).